

§DOI: 10.1002/ ((please add manuscript number))

Progress Report

Progress towards catalytic micro- and nanomotors for biomedical and environmental applications

*Muhammad Safdar, Shahid Ullah Khan, and Janne Jänis**

M. Safdar, S. U. Khan, Prof. J. Jänis
Department of Chemistry, University of Eastern Finland
P.O. Box 111, 80101, Joensuu (Finland)
E-mail: janne.janis@uef.fi

Keywords: micromotor; nanomotor; nanomachines; catalysis; biomedicine; environmental remediation

Abstract: Synthetic micro- and nanomotors (MNM)s are tiny objects that can autonomously move under the influence of an appropriate source of energy, such as a chemical fuel, magnetic field, ultrasound or light. Chemically driven MNMs are composed of or contain certain reactive material(s) that convert chemical energy of a fuel into kinetic energy (motion) of the particles. Several different materials have been explored over the last decade for the preparation of a wide variety of MNMs. In this progress report, we review the discovery of materials and approaches to enhance the efficiency of chemically driven MNMs. We also discuss several prominent applications of the MNMs, especially in the fields of biomedicine and environmental science. The limitations of existing materials and future research directions are also discussed.

1. Introduction

Synthetic micro- and nanomotors (MNM)s have evolved as an exciting research field in materials science and multidisciplinary nanotechnology. The field has gained a part of its inspiration from biological motor proteins, such as kinesin and myosin, that accomplish complex tasks in living cells with a high level of efficiency.^[1] This efficiency has motivated

scientists to develop synthetic counterparts to the biological machinery that could undergo a motion, transport other objects and/or perform catalysis in a similar manner. This has led to the emergence of molecular motors that function as elevators, nanocars, rotors and shuttles etc.^[2-5] The importance of the field was further acknowledged by the Nobel Prize in Chemistry in 2016, awarded to Sauvage, Stoddard and Feringa for the design and production of molecular machines. Beyond an atomic or molecular level actuation, assemblies of molecular machines and the resulting hierarchic structures may demonstrate various macroscale effects, such as self-healing properties, switchable catalysis, drug storage and release and light harvesting.^[6] A progress in the field of molecular motors is thoroughly covered in a recent review,^[7] and will not be discussed in this progress report. Instead, the focus of this article is on “synthetic MNMs”, a term that herein refers to tiny devices composed of a variety of materials, which undergo autonomous motion in liquid environments. Typical dimensions of MNMs can be in the range of few tens of nanometers to several tens of microns, having tubular, wire-like, spherical or anisotropic geometries. The energy required for the motion of MNMs can be provided by the application of a chemical fuel, magnetic field, ultrasound or light.^[8-10] Apart from moving in liquid (aqueous or non-aqueous) environments, MNMs can carry out several different tasks such as catalysis, cargo transport or chemical sensing.^[11-13]

2. Propulsion of MNMs

Motion at very small scale is extremely challenging due to the pronounced viscous effects appearing at a low Reynolds number regime. Hence, the mechanisms of motion adopted by macroscale objects cannot be implemented to impart motion to the micro- or nanoscale particles. Instead, a non-reciprocating movement is required to observe a net displacement. This can be achieved by introducing an asymmetry to the MNMs, which means that an MNM should be made of distinct materials, one of those be a catalyst for a fuel. Janus particles (i.e.,

spherical particles with chemically or physically two distinct faces) possess inherent chemical asymmetry and can be produced following a variety of different methods.^[14,15] Typically, a thin film of a catalyst is deposited on top of silica (SiO₂) or polystyrene (PS) particles to cover their hemisphere. A particle solely made of the catalyst that lacks a chemical asymmetry can also undergo motion if it possesses a certain degree of geometrical asymmetry to facilitate a net effect of the chemical reactions taking place on the overall surface of the particle.

A micro- or nanomotor, which converts a chemical fuel (e.g. hydrogen peroxide, H₂O₂) into reaction products, drives the motion through a few distinct mechanisms. For instance, Pt/SiO₂ Janus particles undergo motion by neutral self-diffusiophoresis.^[16] The catalytic surface of the particle generates neutral reaction products (2H₂O₂ → 2H₂O + O₂), which may have a repulsive interaction with the particle surface. A concentration gradient of the reaction products yields an asymmetric net repulsive interaction with the particle that pushes it forward, as illustrated in Figure 1A. Although Pt/SiO₂ Janus particles are generally believed to be propelled by neutral self-diffusiophoresis, their speeds can be affected in the presence of dissolved ions, which suggests that there is a possibility of multiple mechanisms involved, such as self-electrophoresis or ionic diffusiophoresis.^[17,18] Hence, the overall mechanism is believed to be more complex. On the other hand, the formation of ionic products (e.g. Cl⁻, H⁺, OH⁻ etc.) by colloidal AgCl particles placed under UV light gives rise to another mechanism that is called ionic self-diffusiophoresis.^[19,20] The ionic self-diffusiophoresis is based on the electric and pressure gradients arising from the differential diffusion of specific cations and anions produced by the particle (4AgCl + 2H₂O → 4Ag + 4H⁺ + 4Cl⁻ + O₂), as illustrated in Figure 1B. The metallic Ag produced in the reaction deposits on the particle surface and can be converted back to AgCl by the addition of H₂O₂ (2Ag + H₂O₂ + 2H⁺ + 2Cl⁻ → 2AgCl + 2H₂O).

A propulsion mechanism, which is based on the generation of a local electric field due to an asymmetric formation of ionic products, is known as self-electrophoresis. Self-

electrophoresis is typically exhibited by bimetallic nanomotors, which oxidize hydrogen peroxide (H_2O_2) at the anodic segment (i.e., platinum) and reduce it at the cathodic segment (i.e., gold), thus resembling the action of an electrochemical fuel cell.^[21] As a result, the anodic segment (Pt) produces a higher number of electrons and protons, and an electric field is developed that points towards the cathodic (Au) segment. As the protons migrate towards the cathode, they drag the fluid along, which results in a slip velocity in the opposite direction. The nanomotor thus moves with the anodic segment facing forward (Figure 1C).

Another propulsion mechanism that is more commonly adopted by relatively large particles and tubular geometries is a bubble-induced propulsion. This mechanism is based on the formation of a gaseous product, such as H_2 or O_2 , which forms gas bubbles at the solid–liquid interface. An expulsion of the gas bubbles provides a strong thrust for motion (Figure 1D). This mechanism often requires a small quantity of a surfactant to facilitate bubble formation.

Photocatalytic materials, such as titanium dioxide (TiO_2) can also demonstrate a diffusiophoretic or electrophoretic propulsion, as exemplified in Figure 1E.

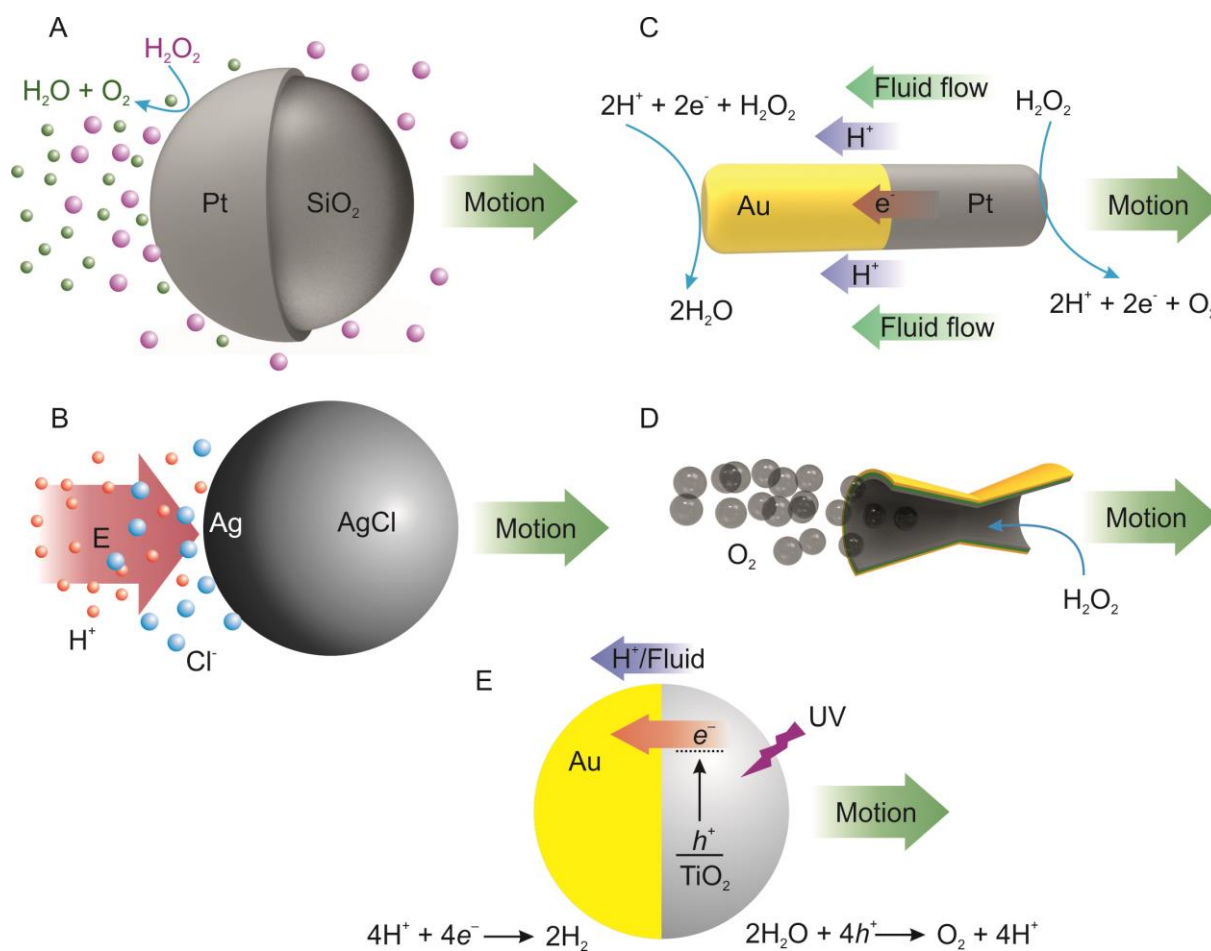


Figure 1. Graphic illustrations of common propulsion mechanism utilized by catalytic MNMs (dimensions not to scale). (A) neutral self-diffusiophoresis, (B) ionic self-diffusiophoresis under UV light, (C) self-electrophoresis, (D) bubble induced propulsion and (E) electrophoretic motion of photocatalytic MNM.

3. Catalytic materials for MNMs

A wide variety of materials has been explored for the preparation of chemically driven MNMs. The motivation behind exploring new materials is often to circumvent the limitations of an existing material, improve the propulsion efficiency or to utilize a new chemical substance as fuel. In the following sections, we review the progress towards chemically driven MNMs from the perspective of materials used for the fabrication and enhancement of the motion efficiency. The MNMs are categorized based on the active materials that drive the

propulsion, and the approaches adopted to improve the propulsion efficiency. This means that MNMs of various geometrical designs will be placed in the same category if they were composed of the same active material. The methods used for the fabrication of MNMs have been recently covered in some excellent reviews and are not discussed here in detail.^[22,23] In **Table 1**, a summary of the catalytic MNMs is presented in respect to the materials used, the particle geometry, the propulsion mechanism, and the typical speed range obtained.

3.1. Platinum-based MNMs

Platinum (Pt) is the most widely used material for the preparation of MNMs owing to its excellent catalytic properties. However, Pt is an extremely rare element, making it among the top ten most expensive metals in the World. Thus, alternative materials to Pt are actively being sought. Pt catalyzes the decomposition of H₂O₂ to produce O₂, which has driven the earliest examples of bubble-propelled microdiscs.^[24] Hemicylindrical plates of the size of <1 cm, composed of a patterned polydimethoxysilane and a Pt surface were placed at the air-fuel interface. The formation of an impulse of bubbles by the Pt surface caused an autonomous motion of the discs with a speed of 1-2 cm s⁻¹. This remarkable observation set the foundation for the development of even smaller self-propelling Pt-based micromotors. Typical MNM device architectures comprising Pt are nanorods, Janus particles and micro-/nanotubes. Due to the large number of developments, which pertain to each of the aforementioned geometrical designs, we will further categorize the Pt-based MNMs according to their geometries.

3.1.1. Nanorods

Nanorods typically have diameters of a couple of hundreds of nanometers and lengths of around a micron. Nanorods are composed of metal segments prepared by electrochemical deposition. Paxton et al. prepared the early example of nanorods composed of Pt and Au segments, by using a template-assisted electrochemical deposition.^[25] When placed in a

solution of H_2O_2 , the motion with a speed of $\sim 10 \mu\text{m s}^{-1}$ occurred without any bubble formation observed. Because the formation of O_2 should take place only at the Pt segment, the authors believed that the generation of an interfacial tension gradient across the Pt and Au segments was responsible for the motion of the nanorods. Later, the authors proposed self-electrophoresis as another possible propulsion mechanism that could propel segmented nanorods.^[21] This was later supported by a strong experimental evidence and it explained the motion behavior of Pt/Au nanorods that move with the Pt end facing forward.^[26,27] The speeds of Pt/Au nanorods were $\sim 20 \mu\text{m s}^{-1}$ in 5% H_2O_2 . Due to the Brownian fluctuations, which constantly alter the orientation and directionality, the trajectories of the nanorods were random. A convenient way to control the directionality of the nanorods is to use an external magnetic field to align and orient the magnetic objects. To accomplish this, nickel (Ni) segments were incorporated to produce Pt/Ni/Au/Ni/Au stripped nanorods.^[28] The magnetized Ni segments allow a precise control over the directional motion, without altering the axial velocity of the nanorods. A further improvement in the efficiency was achieved by the incorporation of carbon nanotubes (CNT) into the Pt segment of the catalytic nanorods.^[29] The doping of the Pt segment with CNTs improved the electron-transfer processes, which resulted in the improved speed of $\sim 43 \mu\text{m s}^{-1}$ in 5% H_2O_2 . Figure 2 A shows the observed trajectories of Pt/Au and CNT-Pt/Au nanorods, their speeds in 15% fuel and a schematic illustration of their propulsion mechanisms. In addition, a mixed H_2O_2 /hydrazine fuel further increased the speeds to $94 \mu\text{m s}^{-1}$ on average. This might be due to hydrazine-induced enhanced catalytic reduction of O_2 and H_2O_2 , and efficient decomposition of hydrazine in the presence of catalytic carbon surface and H_2O_2 . The use of metal alloys is also known to enhance the activity of fuel cell electrodes. A replacement of the pure Au segment with Ag-Au alloy in the Au/Pt nanorods resulted in a 11-fold increase in their speeds as compared to the Au/Pt nanorods.^[30] The composition of the alloy had a strong effect on the catalytic efficiency of the nanomotors. The nanomotors consisting of 75% of Ag and 25% of Au,

showed the fastest motion with an average speed of $87 \mu\text{m s}^{-1}$ in 5% fuel. Besides translational motion, Pt based nanorods may also exhibit rotary motion, based on their design, which should generate an angular torque towards the center of mass (Figure 2 B).^[31,32] Besides improving the propulsion efficiency, a control over the reaction to switch the motion of MNMs “on/off” is also essential to allow their practical use for various applications. In this regard, thermal modulation of the motion of MNMs has been achieved, which takes a simultaneous benefit of the thermal activation of redox reactions and reduction in the viscosity of the surrounding liquid medium.^[33] Alternatively, the electrochemical potential-induced modulation of the motion can be achieved by stepping the potential of a foreign Au electrode placed in the bulk solution containing nanorods.^[34] A negative potential applied to the Au electrode favors faster motion due to the rapid reduction/consumption of local dissolved O_2 . When a potential of -0.4 V was applied, the speeds of the nanomotors increased gradually. An application of a positive potential slowed down the motion, as shown in Figure 2 C.

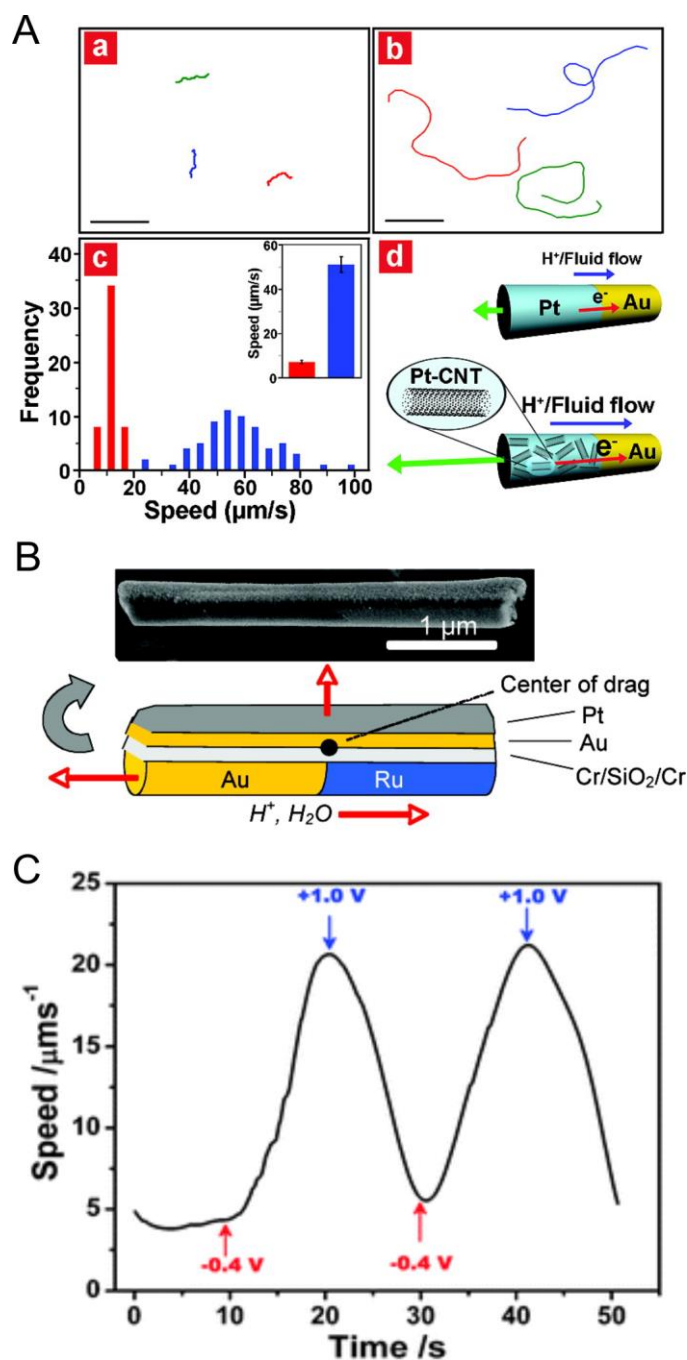


Figure 2. Self-electrophoretically propelled nanorods. (A) CNT doped Pt/Au nanorods vs. the conventional Pt/Au nanorods; (a and b) tracking lines of the conventional Pt/Au nanorods and CNT-Pt/Au nanorods; (c) Histograms of average speeds of Pt/Au (red) and CNT-Pt/Au (blue) nanorods measured in a 15 wt.% hydrogen peroxide fuel. Bar graphs with error bars (inset) represent the mean of average speeds ($\mu\text{m s}^{-1}$) and the error limit at 90% confidence interval of the corresponding nanomotors; (d) schematic representation of the self-electrophoresis mechanism of Pt/Au (top) and CNT-Pt/Au (bottom) bipolar nanomotors with relative arrow lengths indicating the performance. Reproduced with permission.^[29] Copyright 2008, American Chemical Society. (B) catalytic rotor based on vapor deposited layers of Cr, SiO₂,

Cr, Au, and Pt on one side of the Au/Ru nanorods. Reproduced with permission.^[32] Copyright 2009, American Chemical Society. (C) Reversible electrochemical modulation of the Pt/Au nanorod motion upon switching the applied potential (+1.0 to -0.4 V, indicated by arrows) at 10 s intervals in a 5% H₂O₂ solution. The application of -0.4 V led to gradual increase in the speed up to 20 $\mu\text{m s}^{-1}$, which steadily slowed down when +1.0 V was applied. Reproduced with permission.^[34] Copyright 2009, Royal Society of Chemistry.

3.1.2. Janus MNMs

In materials science, the term Janus particle refers to a colloidal particle with two hemispheres having distinct chemical characteristics. Due to their inherent asymmetry, Janus particles offer a great promise for propulsion at the microscale. A variety of fabrication methods exist to prepare Janus particles, which have been recently summarized in the literature.^[15,35] The simplest of all involves deposition of a thin metal film (e.g. Pt) using vapor-phase deposition methods on top of silicon dioxide (SiO₂) or polystyrene (PS) microspheres. Golestanian et al. came up with an earliest model of a self-propelling spherical particle that could undergo a diffusiophoretic motion caused by the asymmetric generation of reaction products.^[36] Later, the findings were experimentally confirmed using Pt coated PS microspheres, which moved at a speed of $\sim 2 \mu\text{m s}^{-1}$ in 5% fuel.^[16] A similar behavior was exhibited by the Pt/SiO₂ particles that were also propelled by diffusiophoresis.^[37] A modification of this approach involved annealing of the Pt coated SiO₂ particles with a thin chromium adhesion layer to produce sphere dimers.^[38] The annealing caused de-wetting of the metallic coating to form a Pt metal particle adhered to the SiO₂ particle. An average speed of $6.0 \pm 4.0 \mu\text{m s}^{-1}$ (in 15% H₂O₂) was achieved from a 70 nm thick Pt coating that produced Pt particles of diameter ~ 450 nm. Gibbs *et al.* found out that the propulsion mechanism of the Pt/SiO₂ Janus particles can be switched from self-diffusiophoresis to self-electrophoresis by first depositing an intermediate Au layer, followed by a dynamic shadowing growth of the Pt layer.^[39] The Pt layer covers a part of the Au layer, allowing the Au segment to be exposed to the fuel, like in the case of bimetallic

nanorods. The Pt/Au/SiO₂ particles underwent faster motion than the Pt/SiO₂ particles, suggesting that the motion by self-electrophoresis is more efficient than by self-diffusiophoresis.

Generally, the motion of spherical Janus particles is subject to a continuous reorientation and change in the directionality under the influence of Brownian effects. A Janus particle in H₂O₂ follow a Brownian-like motion if the observation occurs at a longer time scale but at a shorter timescale, the motion is directional.^[37] The reorientation of the particle due to the rotational diffusion causes a change in the directionality. This necessitates an external magnetic control on the orientation to achieve a directed motion for longer time scales. However, in-plane magnetization achieved in the case of nanorods using a Ni segment cannot be implemented to the spherical Janus particles due to their greater level of geometrical symmetry. Instead, a magnetic layer with the magnetic moment perpendicular to the particle surface should be used. Baraban et al. used [Co/Pt]₅ ultrathin multilayer stack with a Pt top layer to catalytically drive and control the directional motion of SiO₂ microspheres in H₂O₂ solutions.^[40,41] The [Co/Pt]₅ multilayer stack had the magnetic moment oriented along the main symmetry axis of the cap structure, which enabled a precise control over the orientation of the particles. Figure 3 A shows the mean velocity and orientation-dependent controlled motion of Janus particles. A more recent progress to guide the motion of Janus micromotors is based on the use of topographic features.^[42] Pt/SiO₂ particles tend to dock to the edges of the strips, squares and circular posts on a geometrically patterned substrate and move along for several tens of second. Topographically guided motion is a step towards the motion of MNMs along complex pathways without the need for an external magnetic field. Further work can be directed to chemically modify MNMs and the geometrical features of the substrate to tune their surface chemistry by pH or light irradiation, and study their effect on guided motion.

An interesting behavior of the synthetic MNMs, analogous to the swimming bacteria, is their ability to respond to external stimuli, such as pH, light or nutrients. This characteristic is known as “taxis”, and a response to light or chemicals is called as phototaxis or chemotaxis, respectively. Janus Pt/SiO₂ particles show chemotaxis towards high concentration of H₂O₂ due to their translational and rotational diffusion.^[43] Such a behavior can be further investigated by incorporating smart materials onto the MNMs for studying their response, for example, to changes in pH or light intensity.

The Janus microparticles suffer from slow speeds as compared to the nanorods discussed in the previous section. The speed enhancement is a crucial requirement to achieve efficient propulsion. There are several factors that determine the speeds of MNMs such as the catalyst efficiency, the size, surface area and/or geometry of the particles, and viscosity of the used medium. Considering the catalytic efficiency of Pt and the viscosity of the medium being constant under certain conditions, the size and the surface area of the spherical particles can play a decisive role in determining the mechanism of propulsion and the particle speed. Particles with small size (e.g. $\leq 5 \mu\text{m}$) possess larger curvatures that make the nucleation of bubbles very difficult due to larger bubble formation energies.^[44] Thus, by increasing the size of the particles to achieve a smaller curvature, there is a possibility to switch the diffusiophoretic motion into bubble-induced one. Manjare et al. observed that the Janus Pt/SiO₂ particles with a diameter less than $10 \mu\text{m}$ started to undergo quasioscillatory translational motion due to bubble growth and release taking place on the Pt surface.^[45] For smaller structures of $\sim 1 \mu\text{m}$ diameter, a similar translation of the propulsion mechanism was achieved by growing Pt-NPs onto one of the lobes of polystyrene (PS) dimers.^[46] A higher surface area of the Pt-NPs and the resulting surface roughness of the MNM led to the enhanced reaction and bubble nucleation. As a result, the speed enhancement by an order of a magnitude was observed, as compared to the particles coated with a smooth Pt layer. The micromotors designs that combine benefits of smaller curvature and rough morphology with a

high surface area, allow continuous bubble formation and release for a sustained propulsion.^[47]

Besides switching the mechanism to bubble propulsion, the self-diffusiophoretic motion can also be enhanced by adopting certain approaches. For example, a rough Pt layer deposited by glancing angle deposition (GLAD) resulted in a 4-fold increase in the speed when compared to the Janus particles with a smooth Pt surface.^[48] A similar speed enhancement was also observed for graphene-wrapped SiO₂ particles with a Pt layer on top.^[49] The exact mechanism causing this enhancement remains unknown, however.

A modification of the design of conventional Janus MNMs involves a reversed arrangement of the catalytic surface. Instead of depositing Pt at the convex surface of a spherical particle, the concave side of a hollow hemispherical particle can be made from the catalytic material.^[50] Such a configuration provides a straightforward means for selection between enhanced diffusion, self-phoretic or bubble propulsion mechanisms, by simply increasing the particle size.

A greatly modified design of the self-propelled nanomotors was introduced by Wilson et al., who entrapped Pt-NPs inside the polymeric bowl-shaped nano-sized structures serving as the housing.^[51] The motion was believed to have a contribution from the O₂ gas discharge or diffusiophoresis, or both. A similar device architecture was chemically functionalized with temperature responsive poly(N-isopropyl acrylamide) (pNIPAM) polymer chains that widened or narrowed the opening of the nanomotors in response to the changes in temperature (Figure 3 B).^[52] At a temperature around 37 °C, the pNIPAM chains collapsed and the supply of H₂O₂ into the cavity was blocked. When the temperature was lowered to 30 °C, the pNIPAM chains re-swelled to be water soluble, and H₂O₂ fuel could enter into the cavity to propel the motors with an average speed of ~40 μm s⁻¹. Such a temperature-responsive speed regulation of the nanoscale motors is a very promising route to modulate the propulsion for applications requiring a precise control on the locomotive cargo transport and release.

The motion at the nanoscale is even harder than at the microscale due to the dominance of Brownian randomization. Another problem that confronts the motion at the nanoscale is related to the difficulty of realizing anisotropic structures. Nevertheless, the enhanced diffusion coefficient of the enzyme molecules in a substrate solution,^[53] provide evidence that nanoparticles with sufficient asymmetry can also express a similar behavior. Lee et al. confirmed that Pt/Au Janus nanoparticles (~30 or 60 nm in diameter) possessed enhanced diffusion in the presence of H₂O₂.^[54] The motion took place due to self-electrophoresis, like in the case of bimetallic nanorods of a similar composition. Figure 3 C shows the propulsion mechanism and the enhancement of the translational diffusivity in response to the fuel concentration. Silica based nanobottles resembling the shape of a “round bottom flask” were internally decorated with Pt-NPs for nanomotor preparation.^[55] A speed of ~70 μm s⁻¹ in 3% H₂O₂ represents an efficient propulsion for diverse applications.

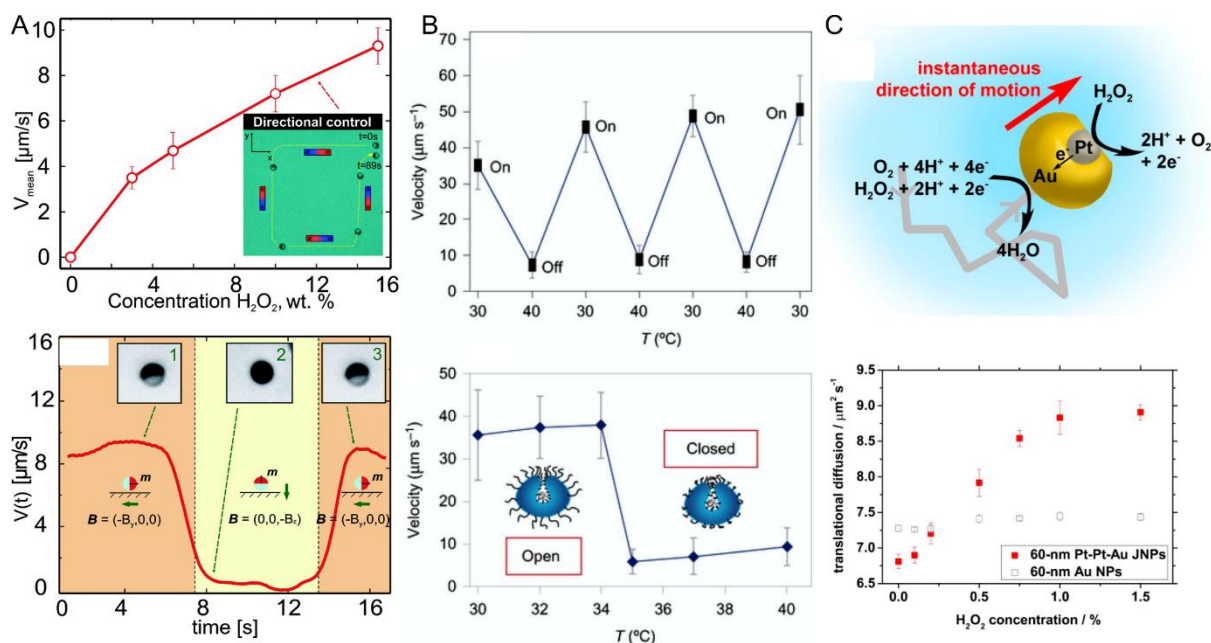


Figure 3. (A) Propulsion and motion control of the Pt/SiO₂ Janus particles with [Co/Pt]₅ ultrathin multilayer stack.; (top) Dependence of the mean velocity of the Janus particles upon H₂O₂ fuel. Inset shows the trajectory and orientation of the particle when guided using an external magnetic field.; (bottom) Controlled motion of the Janus particles is achieved by orienting external magnetic field either in-plane (deterministic propulsion with a certain velocity, regions 1 and 3) or out-of-plane (particle stops, region 2). Reproduced with

permission.^[40] Copyright 2012, American Chemical Society. (B) Motion of the Pt-NPs loaded polymeric nanomotors.; (top) temperature dependent on/off cycles of motion; (bottom) motion in the presence of H₂O₂ at different temperatures illustrates the onset of the collapse of the opening in response to the temperature that stops the motion. Reproduced with permission.^[52] Copyright 2016, Nature Publishing Group. (C) Pt/Au Janus nanomotors.; (top) illustration of self-electrophoresis via catalytic disproportionation of H₂O₂. A gradient of electric charge density generates an electroosmotic flow induced by the charge imbalance, which causes the particle to move in a direction opposite to that of the fluid flow; (bottom) enhancement of the translational diffusion with increasing H₂O₂ concentration. Reproduced with permission.^[54] Copyright 2014, American Chemical Society.

3.1.3. Tubular MNMs

The tubular geometry best suits for the chemically driven MNMs, allowing efficient nucleation and growth of gas bubbles. The inner catalytic surface of a microtube decomposes the fuel into gas bubbles, which rapidly combine and grow into larger bubbles and eventually expel out due to the pressure force. Continuous bubble formation and expulsion in the presence of surfactant provides a strong mechanical force for a fast motion. Solovev et al. introduced tubular mixed metal micromotors composed of Ti/Fe(Co)/Au/Pt, which could propel at a fast speed of $\sim 2 \text{ mm s}^{-1}$ (i.e., 50 body lengths s^{-1}).^[56] The principle of fabrication of the microtubes was based on a stress-induced roll-up technique of the metallic thin films upon the etching of an underlying photoresist layer (Figure 4 A). An increase in the H₂O₂ concentration dropped the bubble radius, while the frequency increased by almost an order of a magnitude. A rather simplified approach to prepare tubular catalytic motors was based on the electrochemical deposition of Pt and Au on the etched Ag wire serving as the template.^[57] The dicing and dissolution of the template produced tubular structures. The propulsion efficiency of these tubular motors was inferior compared to the rolled-up microtubes.

The main shortcoming of the roll-up fabrication approach is the need for a clean-room facility. However, a few methods for the clean-room free fabrication of rolled-up microtubes have been proposed,^[58–60] but their practical applicability is limited due to a poor control on

the fabrication process that results in a polydispersity. A greatly simplified approach to prepare microtubular geometries of precise dimensions is based on template-assisted electrochemical deposition method. Gao et al. reported the synthesis of polyaniline (PANI)/Pt microtubes by using polycarbonate (PC) membranes as the templates.^[61] Because PC is a non-conductor, a thin gold film was deposited onto one side of the template, serving as the electrical contact. The outer PANI layer was electropolymerized to provide a support for the deposition of the catalytic Pt layer. The tubes were recovered by dissolving the template. Figure 4 B shows the fabrication mechanism and the morphology of the PANI/Pt microtubes. The average speed of these microtubes was recorded to be ~ 350 body lengths s^{-1} in 5% of fuel. Besides PANI, other conducting polymers such as polypyrrole (PPy) or poly(3,4-ethylnedioxythiophene) (PEDOT) can also be used as the outer layers. Polymers with varying chain lengths can produce tubes of different inner diameters, which can have a significant effect on the motion behavior.^[62]

The electropolymerized layers of PANI, PEDOT or PPy produce smooth surfaces; hence, the subsequent Pt layer also forms a smooth surface. The propulsion efficiency of electrochemically prepared microtubes can be remarkably improved by depositing a base layer that can facilitate the formation of a rough catalytic surface, such as graphene oxide (GOx).^[63,64] A rough, porous inner Pt surface with a higher surface area and superior catalytic efficiency translates into an efficient motion, requiring very low fuel concentrations. Another effect of the GOx/Pt microtubes with an inner asymmetric microstructure is their unique motion trajectories, as shown in Figure 4 C.^[63] An unbalanced generation of oxygen gas along the porous tubular structures, caused an anisotropic distribution of the drag forces along the axial and radial directions, gives rise to distinct motion patterns.

Moreover, considering a rough inner surface providing an improved performance, the morphology of the outer surface also deserves a careful consideration. A rough exterior surface will experience a greater frictional force that results in a reduction of the observed

speed.^[65] Thus, the surface roughness (inner and outer) is another important parameter to be considered when designing novel MNMs. Another simplistic approach to prepare tubular MNMs is based on the layer-by-layer (LBL) assembly method. Polyelectrolyte materials, such as sodium alginate (ALG) and chitosan (CHI) can be sequentially adsorbed onto the pores of a membrane template, followed by the entrapment of Pt-NPs into the inner most layer.^[66] Solovev et al. observed that it was possible to modulate the motion of microtubes by shining light onto them.^[67] By using rolled-up Ti/Cr/Pt micromotors, the authors noticed a rapid decline in the speed under a white light illumination, which was believed to be caused by the depletion of the fuel and the light-induced degradation of the surfactant close to the Pt surface. Turning the light off was followed by re-initiation of the bubble formation and the motion was restored. The effect of the wavelength of the incoming light illumination on the frequency of bubble formation is shown in Figure 4 D. The motion inhibition at shorter wavelengths was severe as compared to the longer wavelengths. Sanchez et al. evaluated the effect of temperature on the propulsion behavior of the rolled-up micromotors.^[68] The motion was brought to halt at temperatures close to 2 °C, but at physiological temperatures the speed was remarkably enhanced to $\sim 10 \text{ mm s}^{-1}$ (i.e., ~ 200 body lengths s^{-1}) in 5% H_2O_2 . The effect of temperature on the fluid viscosity, speed and motion trajectory is presented in Figure 4 E. The effect of the type of a surfactant on the motion is another important aspect. For example, a surfactant can be anionic (e.g., sodium dodecyl sulfate, SDS), cationic (e.g., cetrimonium bromide, CTAB) or nonionic (e.g., Tween 20). The anionic surfactants are found to facilitate faster motions as compared to the others.^[69] There can be several reasons behind this, such as the varying tendency of adsorption of different surfactants onto the Pt surface, the influence on the frequency of bubble formation or the surface wetting ability. Thus, the selection of a right kind of surfactant is crucial to achieve greater speeds.

3.1.4. Other designs

Bubble propelled MNMs exhibit better motion kinetics than the nanorods or Janus particles driven by self-electrophoresis or diffusiophoresis mechanisms, respectively, as described in the previous sections. A crucial requirement to bubble propulsion is the need of a high-aspect architecture (such as a micro- or nanotube) to allow bubble growth. Janus spherical particles can only allow bubble growth if their size is above a critical value. Huang et al. discovered that hollow, shell-like micromotors with an inner catalytic surface can be propelled by bubble formation.^[70] The authors prepared micromotors with diameters 2–30 μm by using template SiO_2 beads coated with Pt, Ag and Au thin films, and compared their speeds with similar sized Pt/Ti/ SiO_2 Janus motors. The shell-like micromotors moved by bubble propulsion mechanism and were faster than the diffusiophoretically propelled Janus particles of similar dimensions. These motors were chemically asymmetric as the inner and outer surfaces of the motors were Pt and Au, respectively. Later, Pumera's group reported that if a chemical asymmetry is absent, a geometrical asymmetry is sufficient to drive motion of the micromotors.^[71] The Pt shells obtained by dissolving template particles could move by bubble formation that preferentially took place on convex side of the structure.

We prepared two designs of trimetallic microcap-like structures using silica particle templates, which were coated with thin films of Pt/Ni/Au and Au/Ni/Pt to obtain convex and concave catalytic surfaces, respectively.^[72] Surprisingly, no noticeable differences in the speeds were observed, whether the bubble formation took place on the convex or the concave side of the structures. The microcaps could move with an average speed of $\sim 480 \mu\text{m s}^{-1}$ in 6% H_2O_2 , which demonstrates a remarkably fast motion as compared to the Janus MNMs.

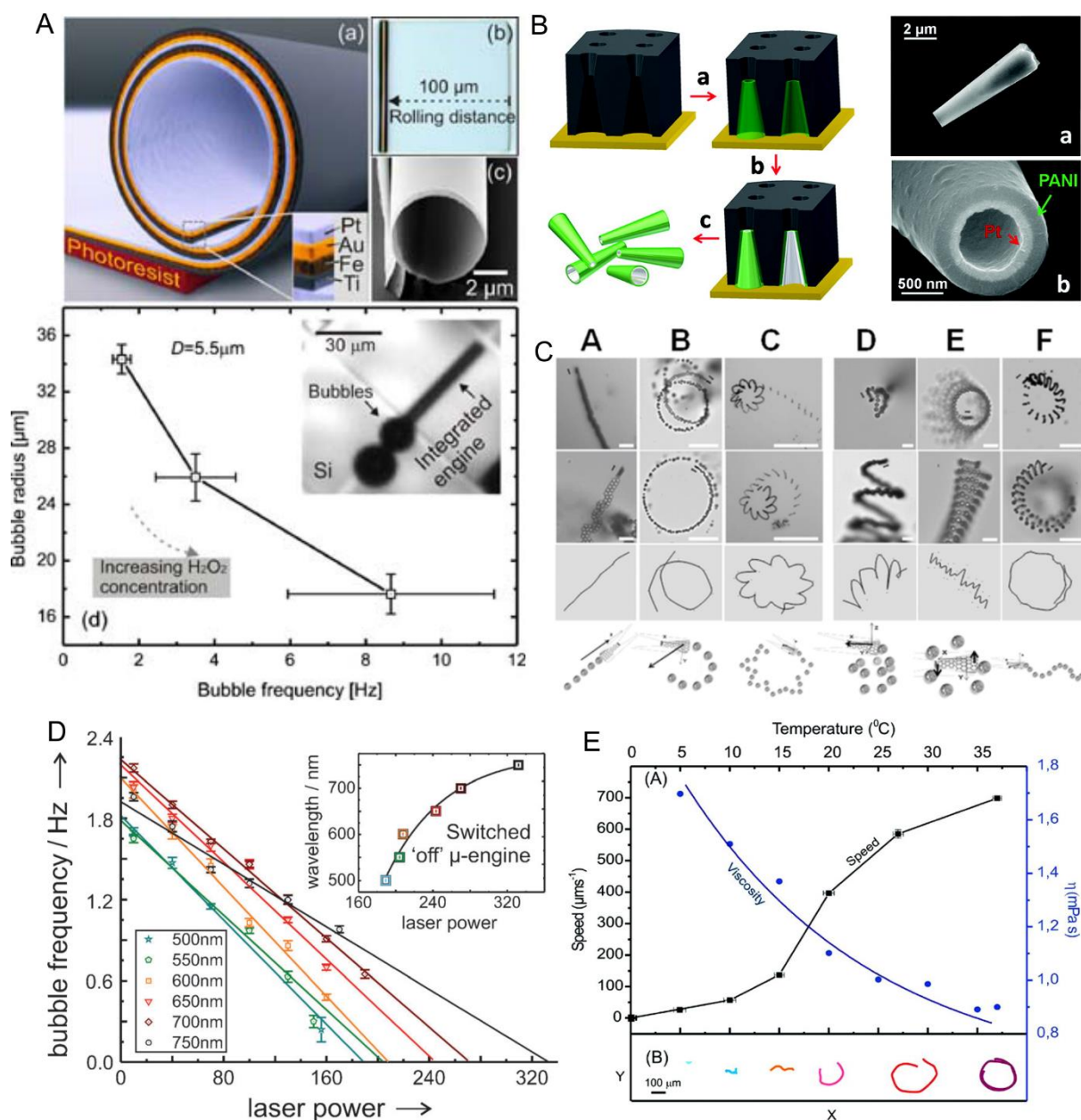


Figure 4. (A) Schematic a rolled-up microtube consisting of Pt/Au/Fe/Ti multilayers on a photoresist sacrificial layer. (top) Optical and SEM images of the rolled-up microtube. (bottom) bubble radius as a function of the bubble frequency with increasing H_2O_2 concentration (from 3 to 15%). The inset shows an optical image of a rolled-up microtube integrated on the Si wafer; Reproduced with permission.^[56] Copyright 2009, Wiley-VCH. (B) Schematic of the template-assisted fabrication of the PANI/Pt bilayer microtubes and SEM images of the released microtubes. Reproduced with permission.^[61] Copyright 2011, American Chemical Society. (C) Optical images of the different motion patterns and trajectories of electrochemically reduced GOx/Pt micromotors, A) linear, B) circular, C) flower-like, D) helical, E) self-rotation, and F) snake-like motions. Reproduced with permission.^[63] Copyright 2015, Wiley-VCH. (D) Dependence of the bubble frequency on the

illuminating wavelength. The straight lines display linear fit functions to experimental data, extrapolated to zero where the micromotors are no longer active. The inset shows a plot of the extrapolated points corresponding to the power required to switch off the motion versus the laser wavelength. Below this curve, the motors are switched off and no microbubbles are observed. Reproduced with permission.^[67] Copyright 2013, Wiley-VCH. (E) Effect of temperature on the propulsion speed of a rolled-up tubular micromotor and fluid viscosity. Reproduced with permission.^[68] Copyright 2011, American Chemical Society.

A serious issue related to the Pt based micromotors is their high cost and severely hindered performance in the presence of salts/electrolytes, proteins and thiol-containing compounds.^[73,74] Thus, the exploration of alternate (cheaper) materials with less limited operating conditions is highly desired.

3.2. Silver-based MNMs

Silver (Ag) is a much cheaper material than Pt, while can similarly decompose H_2O_2 to drive the motion of MNMs. The earliest example of Ag based micromotors was the rolled-up Ti/Fe/Au/Ag microtubes, reported by Mei *et al.* in 2008.^[75] Later, Wang *et al.* discovered that commercially available Ag microparticles can also undergo bubble-induced propulsion.^[76] Even though the particles were chemically symmetric, their structural asymmetry enabled the bubble formation and growth required for motion. The speed $\sim 100 \mu\text{m s}^{-1}$ was reported in 12% H_2O_2 , which refers to a poor bubble formation efficiency at higher fuel concentrations. Amine functionalized polymer particles can be asymmetrically decorated with Ag NPs via forming Pickering emulsion and offer a simple route to create Janus structures that propel by diffusiophoresis.^[77] Polycaprolactone (PCL) based single crystal microstructures decorated with Ag nanoparticles moved at a speed of $\sim 50 \mu\text{m s}^{-1}$ in 10% fuel.^[78] The PCL structures containing thiol groups were first crystallized to form hexagonal single crystals, followed by immobilization of Au-NPs. The Ag-NPs were subsequently deposited onto the Au-NPs via a

silver enhancement procedure. The motion was induced by bubble formation on a single crystal surface. The planer design of these micromotors, which is less favorable for bubble growth, can be one of the possible reasons for their slow speeds. Electrodeposited Ag based microtubes are much more efficient and exhibit an average speed of $\sim 100 \mu\text{m s}^{-1}$, requiring only 1% H_2O_2 .^[79] In this case, the tubular design plays an important role to allow bubble formation. The Janus Ag/Zeolite micromotors with a thin Ag film deposited onto Zeolite microcubes also experienced fast motion with speeds approaching $450 \pm 100 \mu\text{m s}^{-1}$ in 5% fuel.^[80]

As mentioned in section 2, AgCl particles produce a gradient of electrolytes under UV illumination that results in the ionic self-diffusiophoresis mechanism.^[19,20,81] Either a local surface heterogeneity or a non-uniform exposure to the light results in an asymmetric photodecomposition of the particles, which creates an electrolyte gradient. The AgCl particles may reach up a speed of around 100 body lengths (bdl) s^{-1} in water, and demonstrate a schooling behavior. As the reaction continues, a metallic Ag layer on the particle surface causes the motion to halt. Ag_3PO_4 particles exhibit a reversible collective behavior in water in response to an external stimulus, such as NH_3 or UV light irradiation.^[82] The presence of NH_3 generates a stronger outward electroosmotic flow that causes an exclusion behavior of the particles. A similar effect takes place when UV light is turned on. A recent study by Sen and co-workers has reported Ag-Pt bimetallic nanorods that can be powered by self-electrophoresis in the presence of iodine (I_2) as fuel.^[83]

Despite of all the progress towards the Ag based MNMs, the risk of aquatic toxicity due to the release of Ag^+ ions into the environment poses a limitation for their practical use.

3.3. Manganese oxide-based MNMs

Manganese oxide (Mn_yO_x) is an interesting class of catalytic materials that can decompose H_2O_2 in a way similar to Pt. It exists abundantly in the Earth's crust but can also be

synthesized using very low-cost precursor materials. Manganese oxide exists in many different forms (e.g., MnO, MnO₂, MnO₃, Mn₂O₃, Mn₂O₇ and Mn₃O₄), depending on the oxidation state. Manganese oxide is a biocompatible material and does not pose a risk of environmental toxicity. These features make it an attractive choice for the preparation of MNMs to tackle the limitations of Pt and Ag. Wang et al. used commercially available manganese dioxide (MnO₂) particles to observe their motion in H₂O₂ solutions.^[76] A speed of only ~50 μm s⁻¹ required at least 12% fuel, rendering the material poor in catalytic performance. MnO_x/graphene crumples synthesized via an evaporation-induced self-assembly and ultrasonic spray pyrolysis method, could push a 3D printed boat-like structure due to a strong thrust provided by the bubbles.^[84] An SEM image of the crumple is shown in Figure 5 A. The Mn_yO_x was polycrystalline in nature and was composed of Mn₃O₄ and MnO₂. Feng et al. used hydrothermal synthesis to prepare sandwich-like MnO₂/graphene flakes with MnO₂ nanosheets anchored to both sides of the graphene layers (Figure 5 B).^[85] The α-MnO₂ constituting the composite flakes demonstrated efficient propulsion with a speed ~16 μm s⁻¹ in only 0.15% H₂O₂. The speed increased from 23 to 111 μm s⁻¹ in 2.5% fuel as the size of the flakes was decreased from 10 to 4 μm, but the lifetime of the micromotors was only around 2 min. The short lifetime of the MnO_x based MNMs is due to their dissolution/degradation in H₂O₂ solutions. Recently reported paper-based tubular microjets coated with MnO₂ nanoparticles required at least 9% H₂O₂ to become motile, and could gain a maximum speed of ~2 body lengths s⁻¹ with a lifetime of 6 min in 16% fuel.^[86] The preparation of paper microjets was performed by printing a sheet of paper with a magnetic ink, followed by soaking the paper in the KMnO₄ solution, as shown in Figure 5 C. Manganese based MnFe₂O₄ pot-like hollow microparticles are an example of another interesting design that facilitates bubble formation at the inner catalytic surface.^[87] An SEM image of the sliced MnFe₂O₄ particle is shown in Figure 5 D. Although, both the inner and outer surfaces of the

particles were catalytically active, a high concentration of the generated O_2 molecules confined inside the particle could form bubbles to drive motion.

Manganese oxide exists in a wide range of crystalline forms (polymorphs) and their catalytic efficiency differs on the basis of their crystalline structure. For example, MnO_2 exists in many different crystalline forms, including α - MnO_2 , β - MnO_2 , γ - MnO_2 and ε - MnO_2 . In addition, MnO_2 can be prepared via various synthesis methods, which produce distinct geometrical shapes (e.g. tubular, rod-shaped, spherical etc.), and different methods of synthesis may produce distinct polymorphs. We recently reported the effect of geometrical designs and polymorphs on the motion behavior of Mn_yO_x based micromotors.^[88,89] Tubular and rod-like structures were prepared by template-assisted electrochemical deposition method, which produced amorphous MnO_2 and were the least active in terms of their speeds. Spherical particles made of Mn_2O_3 and birnessite-type MnO_2 showed higher velocities. The highest performance and the longest lifetime (≥ 40 min) was observed with ε - MnO_2 , irrespective of whether the particles were synthetic or obtained commercially. The surface morphology of the particles is shown in Figure 5 E. Wang and coworkers reported PEDOT/ MnO_2 microtubes of 2 μm diameter what could propel even in 0.4% fuel, and the speeds reached 319 $\mu m s^{-1}$ in 10% H_2O_2 .^[90] The improved efficiency of propulsion at low fuel concentrations might be due to the formation of α - MnO_2 , as also shown for the previous hydrothermally synthesized MnO_2 /graphene flakes.^[85] However, the formation of α - MnO_2 by electrochemical deposition method is contrary to our previous observation,^[89] and the factors responsible for this discrepancy are not known. Hence, the resulting crystalline form of MnO_2 has a strong impact on the performance and should be given a consideration while designing Mn-based MNMs.

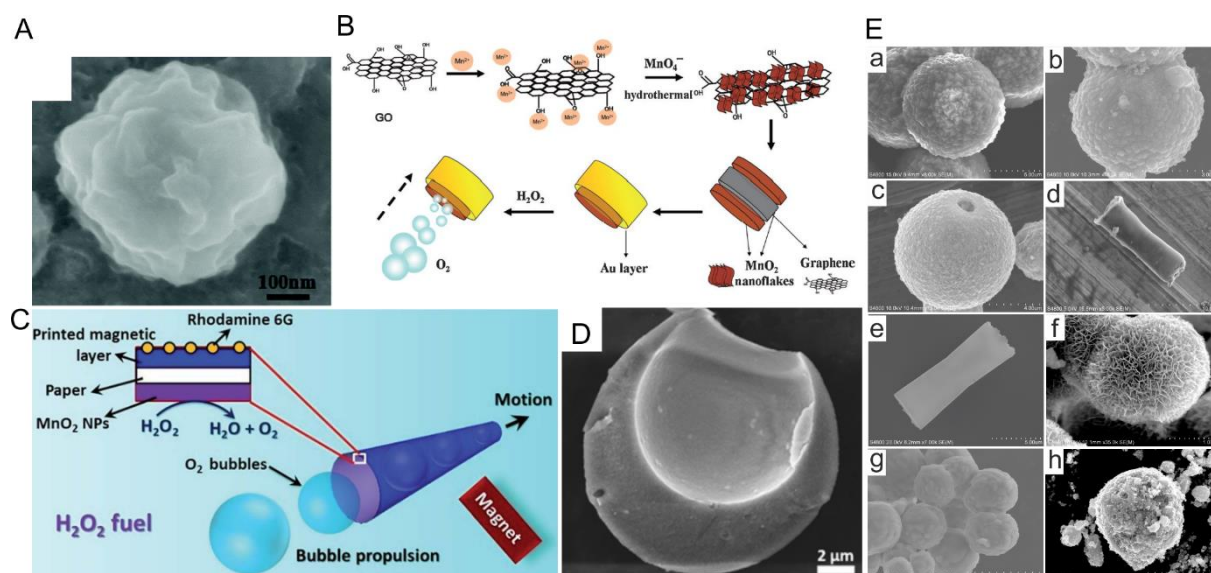


Figure 5. (A) SEM image of the MnO_x/graphene crumple. Reproduced with permission.^[84] Copyright 2014, Royal Society of Chemistry. (B) Schematic of the fabrication and operation of MnO₂/graphene flakes prepared by hydrothermal synthesis. Reproduced with permission.^[85] Copyright 2015, The Chemical Society of Japan. (C) Illustration of paper based micromotors decorated with MnO₂ NPs. Reproduced with permission.^[86] Copyright 2015, Royal Society of Chemistry. (D) SEM image of a sliced MnFe₂O₄ pot-like hollow microparticle. Reproduced with permission.^[87] Copyright 2015, Wiley-VCH. (E) SEM images of (a) MnCO₃ template particle, (b) ε-MnO₂@MnCO₃, (c) ε-MnO₂ hollow, (d,e) PEDOT/MnO₂ microtube and MnO₂ microrod, (f) birnessite-type MnO₂, (g) Mn₂O₃ and (h) commercial MnO₂ identified as ε-MnO₂. Reproduced with permission.^[89] Copyright 2016, American Chemical Society.

3.4. Zinc- and magnesium-based MNMs

The main limitation of the materials discussed so far is the requirement of toxic fuels for motion, such as hydrazine or H₂O₂. Thus, alternate materials that could utilize non-toxic, biocompatible fuels are highly desired. For example, materials with a more negative redox potential as compared to H₂ can generate H₂ gas. For example, zinc (Zn) is widely used for the production of hydrogen energy.^[91] In comparison to the alkali metals that also lead to H₂ generation upon hydration, Zn is very safe and can be electrochemically deposited. The first demonstration of bubble-propelled micromotors utilizing H₂ gas was reported by Gao et al.^[92]

The microtubular motors comprising PANI/Zn layers were propelled in different acid solutions with varying speeds based on the dissociation constants of the acids. At an extremely low pH of -0.2 , an ultrafast speed of $1050 \mu\text{m s}^{-1}$ was observed using HCl as an acid. Due to the rapid oxidation and dissolution of Zn in acidic environments, the micromotors had a lifetime of only a few minutes, which was strongly dependent on pH. The optical images of moving PANI/Zn micromotors and the effect of pH and microtubular dimensions on the speed is shown in Figure 6 A. The micromotors of smaller dimensions moved relatively slowly than the ones with a wider opening and a greater length. In addition to serving as a base, the PANI layer serves as a protecting coating for Zn, so that the reaction only takes place at the end of the microtubes. The deposition of Zn without an external base layer forms rod-shaped microstructures that are inferior in terms of speeds.^[93] The maximum operational lifetime of rod-like motors was only 5 s, because the Zn surface was fully exposed to the solvent, which causes a rapid dissolution of the material. The micromotors with relatively larger dimensions (corresponding to the larger quantity of Zn), with an outer PEDOT layer, could operate for up to 10 min at pH 2.^[94]

Magnesium (Mg) is another biocompatible and low-cost material, which possesses a tendency to reduce water and evolve H_2 . Under the ambient conditions, the surface of Mg particles is covered by a hydroxide passivation layer, which protects Mg from reaction with water. The dissolution of the passivation layer in aqueous sodium bicarbonate or sodium chloride solution triggers Mg hydration to produce a burst of hydrogen bubbles that can propel Mg particles.^[95,96] The Mg particles can move with speeds reaching few body lengths s^{-1} . Mg particles can be obtained commercially in bulk quantities and their surface can be modified, by depositing a thin metal film to the particles, to make Janus structures.

3.5. Nickel- and iridium-based MNMs

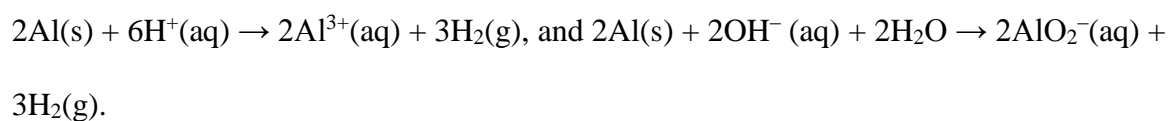
Nickel possess a tendency to decompose H_2O_2 but far less efficiently than the materials discusses in the previous sections. Nanorods composed of Ni/Au segments show a rotational motion when the Au segment was anchored to the Si substrate.^[97] These rotors were clocked at a constant speed of $\sim 1.5 \text{ rad s}^{-1}$. An autonomous motion of the untethered nanorods was also observed that underwent a movement in a circular orbit. The efficiency of Ni catalyst was improved by forming a Ni-Fe alloy for the Au-Fe/Ni nanowires that led to a directional motion with the speed up to $369 \mu\text{m s}^{-1}$ in 10% H_2O_2 and 0.06% hydrazine.^[98] Here, the presence of both the hydrazine and H_2O_2 was necessary for a motion. The role of hydrazine was to co-catalyze the decomposition of H_2O_2 .

Iridium (Ir) decomposes hydrazine (N_2H_4) to form N_2 , NH_3 and H_2 , and is another candidate for the preparation of MNMs. Janus Ir/ SiO_2 particles are propelled by self-diffusiophoresis, similar to their Pt counterparts (Figure 6 B).^[99] When compared to Pt/ SiO_2 particles that move at a speed of $12 \mu\text{m s}^{-1}$ in 10% H_2O_2 , the Ir/ SiO_2 particles can reach a speed of $20 \mu\text{m s}^{-1}$ in just 0.001% N_2H_4 , representing an exceptional catalytic efficiency.

3.6. Aluminum-based MNMs

Like Mg, aluminum (Al) can reduce water to form H_2 , but the reaction is hindered by the passivation layer that is quickly formed onto the bare aluminum surface in a reaction with oxygen. Alloys of Al with Ga can react with water because Ga can penetrate the Al surface to remove the oxide layer. The reaction can be shown as follows: $2\text{Al} + 6\text{H}_2\text{O} \rightarrow 3\text{H}_2 + 2\text{Al}(\text{OH})_3$. Janus Ga-Al/Ti microparticles prepared by Gao et al. achieved fast speeds of up to $\sim 3 \text{ mm s}^{-1}$ in water with a lifetime of over 5 min.^[100] The water splitting reaction efficiently took place in acidic and basic environments, and in various other media such as serum and cell culture medium. The passivation layer can also be dissolved by a strong acid or base to allow for H_2 evolution reaction. The Janus Pd/Al particles can propel in acidic as well as in basic aqueous environments due to the reaction of the Al segment, whereas the Pd surface can

drive motion in the reverse direction in the presence of H_2O_2 , making Pd/Al a multi-fuel driven microsystem.^[101] The reaction of Al in the acidic and basic solution are as follows:



3.7. Ruthenium-based MNMs

Catalytic decomposition of H_2O_2 by Ru metal has allowed Au-Ru nanorods to propel with the Au end facing forward.^[102] This is in contrast to the Au-Pt nanorods, which move in the direction of the catalytic Pt segment. The dipolar electric field generated by proton gradient around the Au-Ru nanorods triggers a dynamic assembly into pairs and triplets. Nanotubes composed of Au-Ru segments propel faster as compared to the nanorods of similar composition, due to the generation of a higher proton flux from the inner and outer catalytic surfaces of the tubes.^[103] Trimetallic nanorods with alternating Au and Ru segments oxidize and reduce H_2O_2 at the Au and Ru segments, for an autonomous propulsion.^[104] The hydrodynamic and electrostatic forces operating at short and long distances, respectively, contribute to the reorientations and assembly of the particles. Polyelectrolyte microcapsules loaded with ruthenium polyoxometalate (Ru_4POM) complex present another strategy to synthesize self-propelling micromotors.^[105] Figure 6 C illustrates the composition of the polyelectrolyte multilayer capsule with loaded Ru_4POM complexes, prepared by the layer-by-layer assembly.

3.8. Metal organic framework-based MNMs

Functional materials based on metal-organic frameworks (MOFs) offer another unique way to design catalytic MNMs. MOFs are microporous crystalline materials with tunable properties and applications in various fields, such as drug delivery, separation science and catalysis.^[106] MOFs composed of zeolite imidazolate frameworks (ZIF-8/ZIF-67 Janus with redox active Co^{2+}) and University of Oslo (UiO)-type scaffolds (UiO-67 metalated with Co^{2+} and Mn^{2+})

have shown a promise for H₂O₂-driven MNM fabrication (Figure 6 D, E).^[107,108] The motion of these MNMs can be modulated using chelating agents that can bind and remove the active metal content from the MOF architecture, which results in the loss of motion. Future studies should be directed to improve the propulsion efficiency of these materials for an operation at low levels of fuel.

3.9. Iron-based MNMs

Metallic iron (Fe) also slowly reacts with water due to the instantly formed oxide passivation layer. However, a reaction with an acid can form H₂ bubbles, which may impart sufficient driving force to the particles for autonomous propulsion. The Fe-NP aggregates submerged in an aqueous solution of 3.38 wt.% citric acid and 1% SDS moved with a speed of 7–20 μm s⁻¹.^[109] The electrodeposited multilayered PEDOT/Au/Fe based micromotors propelled by reaction with 1.2M HCl to the speed of ~35 μm s⁻¹.^[110] The chemical reaction involved is represented as: $\text{Fe(s)} + 2\text{H}_3\text{O}^+ \rightarrow \text{Fe}^{2+}(\text{aq}) + 2\text{H}_2\text{O} + \text{H}_2(\text{g})$. The ferromagnetic character of Fe offers an additional benefit to control the directionality of propulsion through an external magnetic field.

3.10. Calcium-based MNMs

The controlled reaction of calcium carbide (CaC₂) with water produces acetylene gas that can power up CaC₂ particles: $\text{CaC}_2(\text{s}) + 2\text{H}_2\text{O}(\text{l}) \rightarrow \text{Ca}(\text{OH})_2(\text{s}) + \text{C}_2\text{H}_2(\text{g})$. To achieve a control over the reaction, the CaC₂ granules can be encapsulated in thin porous polymeric film.^[111] The water seeping past the polymer membrane leads to a rapid evolution of gas bubbles which aid a buoyancy effect and a translation motion across the air/water interface. The water Effervescent drug delivery systems based on carbonates (e.g. calcium carbonate) are also of interest for the preparation of MNMs due to their reaction with mildly acidic solutions to form gas bubbles. Janus calcium carbonate particles experience a directed motion at pH 6.5, but

with a rather slow speed (ca. $1.8 \mu\text{m s}^{-1}$).^[112] The motion takes place due to the controlled dissolution of CaCO_3 particles. Despite the slow speeds, the self-propulsion in a mildly acidic environment is a considerable advancement towards potential future applications.

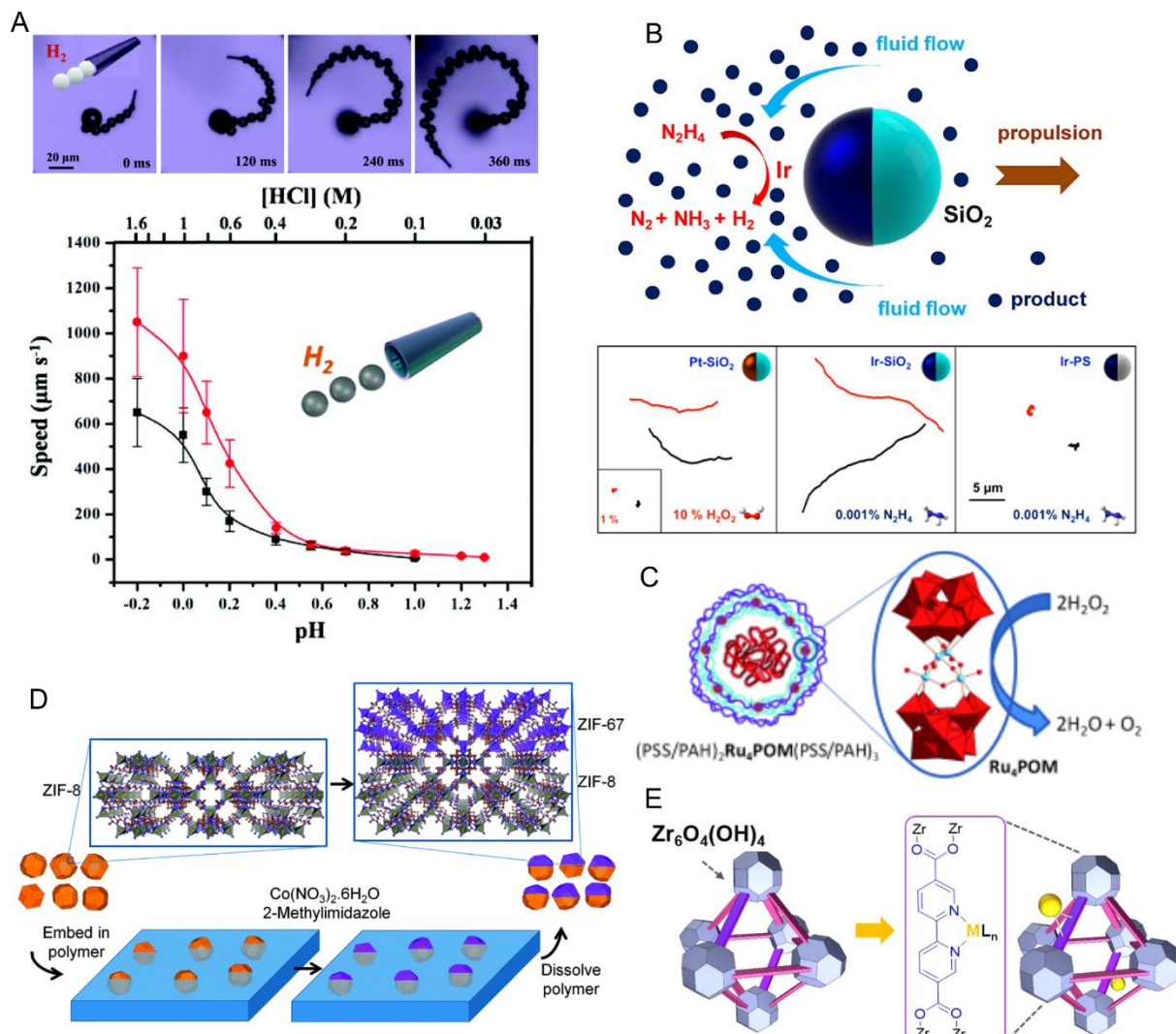


Figure 6. (A) PANI/Zn micromotors driven by HCl solution. (top) time-lapse optical images of the motion of Zn micromotors.; (bottom) pH dependence of the speeds in solutions of different HCl concentrations. Red and black curves represent micromotors with 5 and 2 μm diameter, respectively. Reproduced with permission.^[92] Copyright 2012, American Chemical Society. (B) Iridium based Janus micromotors.; illustration of the propulsion mechanism and trajectories of Pt/SiO₂, Ir/SiO₂ and Ir/PS Janus particles in the presence of 10% (inset) H₂O₂ fuel, and 0.001% N₂H₄ fuel, respectively. Reproduced with permission.^[99] Copyright 2014, American Chemical Society. (C) illustration of the polyelectrolyte/polyoxometalate (Ru₄POM) complex based micromotors. Reproduced with permission.^[105] Copyright 2014, Wiley-VCH. (D) schematic of the preparation of Janus ZIF-8/ZIF-67 MOF motors.

Reproduced with permission.^[107] Copyright 2014, Royal Society of Chemistry. (E) schematic of the metalation of UiO-67 MOF (M = Co, Mn). Reproduced with permission.^[108] Copyright 2017, American Chemical Society.

3.11. Enzyme-based MNMs

Enzymes are biomacromolecules that catalyze various biochemical reactions in a highly specific and efficient manner. The use of enzymes in the fabrication of synthetic MNMs is inspired from their high activity and biocompatibility. Several different enzymes are commercially available and a variety of immobilization techniques exist, which makes the fabrication of enzyme-based MNMs straightforward. For example, catalase can be regarded as a biological alternate to Pt, Ag or MnO₂, because it decomposes H₂O₂ into oxygen and water molecules.

The earliest example of enzyme-driven MNMs was based on the use of a covalently tethered synthetic catalase mimic.^[113] The immobilization of the enzyme mimic took place by the p-formyl-functionalized complex via covalent coupling of the bridging carboxylate ligand to the aminopropyl-modified SiO₂ microparticles. The speed of the microparticles were measured to be 35 μm s⁻¹ in the presence of 5% H₂O₂. Sanchez et al. immobilized natural catalase inside the Ti/Au rolled-up microtubes, having surface modified with a monolayer of 3-mercaptopropionic acid.^[114] These micromotors moved by bubble propulsion and reached a speed of ~226 μm s⁻¹ in 1.5% H₂O₂ (Figure 7 A). A similar strategy was adopted to immobilize catalase inside the electrodeposited polypyrrole/Au microtubes.^[62] Silica (SiO₂) particles functionalized with amino or carboxylic acid groups offer another simple route to immobilize catalase.^[115,116] However, the immobilized enzymes are prone to gradual loss of the activity, possibly due to chemical treatment or undesired interactions with the base material. In addition, a long-term operation in high H₂O₂ concentrations can also cause deactivation of the catalase through peroxide-induced structural changes. This issue can be

addressed by encapsulating the enzymes in polymeric shells by acrylation and polymerization steps. The resulting enzyme capsules can be grafted onto the surface functionalized microparticles to produce micromotors with long lasting operational capability.^[117] Catalase is also an essential part of the defense system of living cells because of its scavenging action against reactive oxygen species and free radicals.^[118] Several plants express catalase with varying levels of activity and its distribution may spatially vary throughout the structure of the plant tissues. Millimeter sized segments of potato or cherry-belle radish tissues rich with catalase have demonstrated bubble-induced motion in H₂O₂ solutions for up to 2 min.^[119,120]

The enhancement of diffusivity of single enzyme molecules in the substrate solution increases as the substrate concentration is increased, which refers to the fact that the individual enzyme molecules can act as nanomotors.^[53,121,122] When bound to a static surface, enzymes can act as micropumps that generate a fluid flow to drive colloidal particles.^[123] The requirement of cytotoxic fuels such as H₂O₂ to drive MNMs impedes their potential for biological applications. Using a binary enzyme system, this problem can be overcome. For instance, glucose oxidase (GluOx) and catalase immobilized/entrapped MNMs can be powered by supplying a solution of glucose.^[124–126] GluOx converts glucose into H₂O₂ as a reaction byproduct, which can then be utilized by catalase (or Pt-NPs)^[127] as an *in situ* produced fuel to power MNMs. Figure 7 B shows schematic of an enzyme loaded supramolecular nanomotor.^[126]

Submicron particles with immobilized urease show an enhanced diffusion in urea solutions, making it an excellent enzyme of choice for the preparation of fully biocompatible MNMs.^[128,129] Ma et al. recently demonstrated a controlled chemophoretic propulsion of hollow mesoporous silica Janus particles with an immobilized urease.^[130] A modulation of the particle velocity was achieved by chemically inhibiting and further reactivating the enzyme, by adding Ag⁺ or Hg²⁺ ions and dithiothreitol (DTT), respectively. The motion was possible

under physiological conditions (i.e. 5-10 mM urea) with speeds approaching $\sim 10 \mu\text{m s}^{-1}$.

Figure 7 C presents the “on/off” motion control and dependence of the speed on urea concentration. Tubular silica nanojets with an immobilized urease also exhibited a similar type of bubble-free rotational and translational propulsion.^[131] These studies suggest a huge potential of urease to drive MNMs of distinct geometrical designs.

Peptides and proteins are abundant biomolecules that are present in every living organism. The use of natural proteases, such as trypsin or pepsin, represents another promising route to design MNMs that could asymmetrically decompose/cleave peptides into smaller byproducts. Trypsin immobilized Janus particles have shown an enhanced diffusivity in a solution of rhodamine-110 bis(benzyloxycarbonyl-L-arginine amide) conjugate (BA-Rho-110) as the model peptide fuel (Figure 7 D).^[127] Trypsin cleaves peptide bonds at the C-terminal side of arginine and lysine residues. The instantaneous velocity of the particles increased by roughly 8 times, from $0.04 \mu\text{m s}^{-1}$ (no fuel) to $0.33 \mu\text{m s}^{-1}$ upon exposure to 200 μM peptide substrate. To this end, the progress is certainly intriguing, but further studies are required using different peptides and investigating the effect of peptide length on motion.

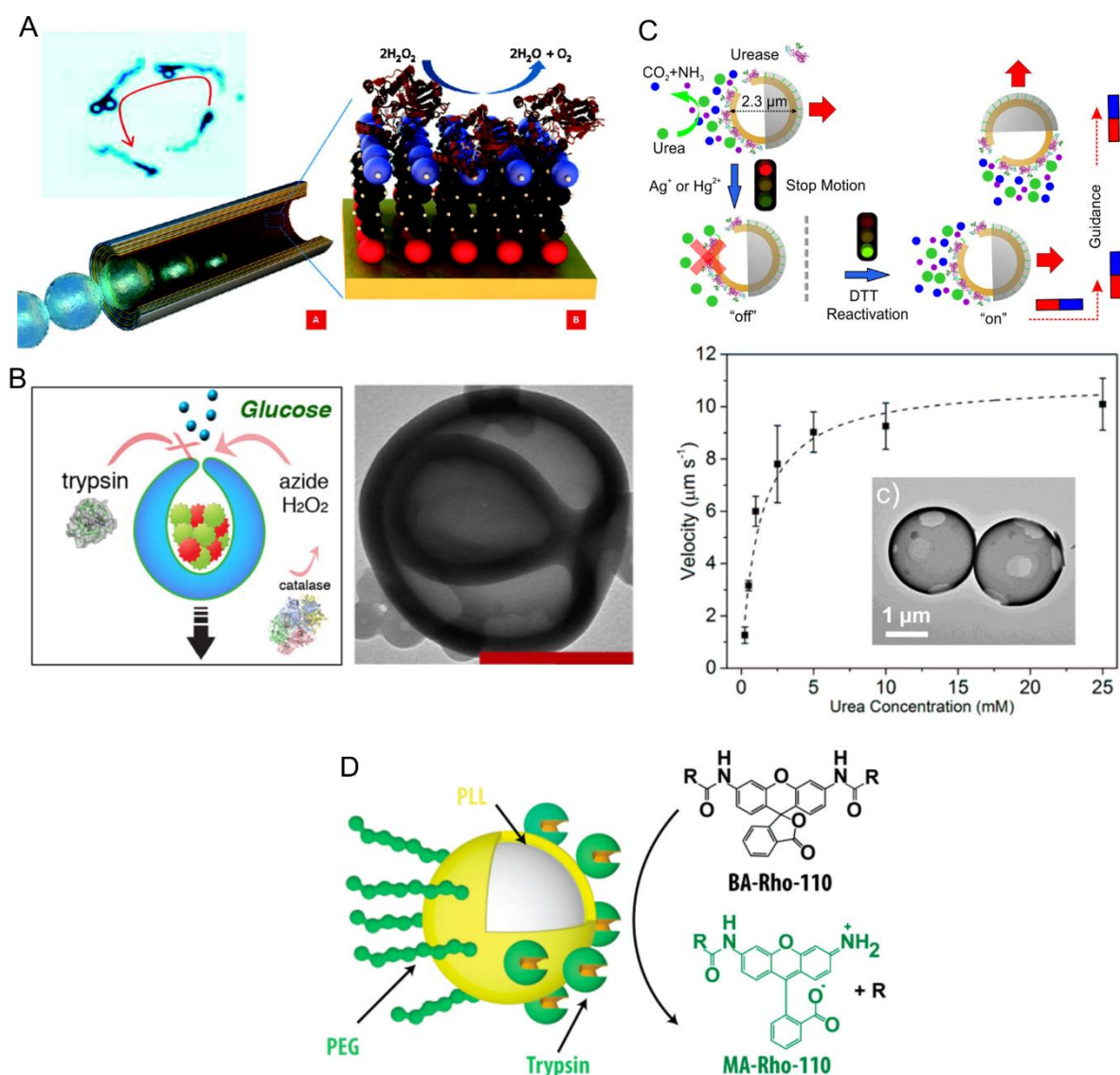


Figure 7. (A) Schematic of the Ti/Au rolled-up microtubes with immobilized catalase. Inset shows an optical image of the moving microtube. Reproduced with permission.^[114] Copyright 2010, American Chemical Society. (B) Enzyme loaded supramolecular nanomotors. Schematic representation of the size-dependent inhibition and protection of the binary enzyme based supramolecular nanomotor. A small inhibitor sodium azide can diffuse inside the nanomotor to deactivate the enzyme, while large proteases cannot enter. TEM image of a supramolecular nanomotor is also shown. Reproduced with permission.^[126] Copyright 2016, American Chemical Society. (C) Urease immobilized Janus hollow mesoporous particles. (top) motion and directionality control using inhibitors, reactivator and external magnet, respectively.; (bottom) plot of velocity vs. urea concentration. Inset shows TEM image of the hollow particles. Reproduced with permission.^[130] Copyright 2016, American Chemical

Society. (D) Illustration of the trypsin based micromotor. Reproduced with permission.^[127]
Copyright 2017, American Chemical Society.

3.12. Titanium oxide and related photocatalyst-based MNMs

Titanium dioxide (TiO₂) is an efficient photocatalyst with interesting features like low cost, high chemical stability, high refractive index and good biocompatibility. TiO₂ is widely used in biomedical science, photocatalysis and energy conversion applications.^[132,133] We recently reviewed the progress of light-driven MNMs (including TiO₂ and related photocatalysts), therefore only a brief summary is given here.^[134] The photocatalytic reactions on TiO₂ surface take place when photons of a sufficient energy create a separation of electrons and holes in the material. A small fraction of the highly reactive species, which manage to escape from the recombination zone, reaches the particle surface to react with the surrounding chemicals and form ionic products to drive the motion. An early report on the TiO₂-based MNMs used commercially available anatase-TiO₂ particles, which underwent a motion when irradiated with a 365-nm UV light.^[135] Here, the motion was caused by a combined effect of diffusiophoresis and osmophoresis. Later studies observed active propulsion of the tubular TiO₂ structures.^[136–138] As TiO₂ exists in the form of different crystalline phases, propulsion efficiency of TiO₂-based MNMs may vary, similar to that observed with the MnO₂-based MNMs, discussed previously. Bimaterial colloids composed of haematite/TiO₂ can photocatalytically degrade H₂O₂, which creates an osmotic self-propulsion and a phoretic attraction between them.^[139] This results in a collective behavior that involves a formation and deformation of the particle ensembles.

The coating of TiO₂ particles with a thin Au film is known to improve photocatalysis, and MNMs can certainly benefit from it.^[140] TiO₂/Au Janus particles undergo rapid motion in water under UV light, with speed reaching 25 bdl s⁻¹.^[141] A further increase of the speed can be achieved by adding a small quantity of H₂O₂ that enhances the electrophoretic effect of TiO₂/Au particles. A similar mechanism is also shown by Janus TiO₂/Si nanotree structures,

partly decorated with Pt-NPs, which can self-align with the direction of light propagation.^[142] By chemical modification of the structures, the zeta potential of the photoanode can be controlled to program a particle to exhibit either positive or negative phototaxis. In contrast to the previously described AgCl particles that also show a collective behavior but undergo a gradual decomposition, TiO₂ particles do not undergo degradation and can form non-equilibrium ensembles for as long as the UV light is present. Mark *et al.* have used anatase-TiO₂/SiO₂ Janus particles to create dynamic colloidal crystals and assemblies of passive SiO₂ particles with various shapes and sizes.^[143] The motion of Janus particles takes place via self-diffusiophoresis originating from the photodecomposition of H₂O₂ at the TiO₂ surface due to the UV promoted electron-hole pairs.

4. Applications of micro and nanomotors

4.1. Cargo transport

Biological motor proteins actively perform intracellular transport of vesicles and organelles along the predefined pathways, called microtubule filaments. This inspired the earlier proof-of-concept applications of the synthetic MNMs to pick-up, transport and deliver model cargo systems, such as nano/microparticles.^[144] The modified Pt/Au nanorods were anchored to the polystyrene (PS)-amidine and PS-streptavidin microspheres via electrostatic and biotin-streptavidin interactions, respectively (Figure 8 A). The self-electrophoresis mechanism drove the transport of various sizes of cargo particles. The speeds of the individual MNMs decreased as the size of cargo particles increased, owing to the simultaneous increase in the viscous drag. Similar nanorods with a Ni segment for directional control and magnetic cargo-towing could navigate through a microchannel network.^[145,146] The release of the cargo particles was triggered by rapidly reversing the direction of the nanomotor by using an external magnet. Due to the fast reversal in the direction, the drag force on the particle

overcomes the magnetic attraction between the particle and the Ni segment and the particle is released. The propulsion speed inside the microchannels was inferior as compared to the outer side of the channel.

Another way of releasing the cargo involves the incorporation of an Ag segment between the Pt and Au segments of the Pt/Au/Ag/Au nanorods, or using a photocleavable linker to bind biotin functionalized cargo to the Pt-Au-PPy-PPyCOOH nanorods.^[147] In the former case, the Ag segment can be dissolved to release the cargo. The metallic nanorods, however, suffer from poor power output and their incompatibility with electrolytes and ionic environments, which limits their cargo towing ability.

Spherical Pt/PS Janus particles form aggregates with bare PS particles due to van der Waals forces and carry them along, whereas, magnetic Janus Pt/SiO₂ particles can manipulate superparamagnetic beads.^[40,148] A magnetic control over the orientation of Janus particles enables a precise directional guidance inside a complex microfluidic network to selectively pick and transport the cargo, sorting of particles and pushing ensembles of colloidal particles (Figure 8 B).

Microtubular motors have also demonstrated several interesting specific and nonspecific cargo transport applications. An example of nonspecific transport is pushing the particles and cells forward.^[149,150] In Figure 8 C, D, microtubular motors are shown to push cells and colloidal cargo particles, respectively. On the other hand, a specific cargo transport requires biochemically modified motors with specific recognition sites for the binding of a certain cargo (e.g. cancer cells, proteins, bacteria, sugars etc.).^[151–156] Ferromagnetic microtubes can selectively pick up and separate paramagnetic beads from a mixture of particles without any surface modification.^[157]

4.2. Biomedical applications

Conventional drug delivery systems are based on passive distribution of therapeutic agents inside the body. The blood carries drug molecules not only to the unhealthy organs but also to the health ones. These systems lack a proper drug targeting and tissue penetration ability for localized release of the therapeutics only to the unhealthy cells.^[10] Thus, self-propelling MNMs hold exciting prospects to actively deliver drug therapeutics to target sites due to their motion, directional control and tissue retention/penetration ability. For instance, mesoporous silica NPs with a Pt cap were loaded with a chemotherapeutic drug doxorubicin (DOX) for active intracellular drug release.^[158] Polymeric stomatocyte nanomotors made of soft self-assembled block copolymers, based on poly(ethylene glycol)-b-polystyrene and poly(ethylene glycol)-b-poly(ϵ -caprolactone), were loaded with Pt-NPs and DOX for active drug release to the cancer cells.^[159,160] An illustration of the stomatocyte nanomotor with loaded Pt-NPs and DOX is presented in Figure 8 E.

Zn and Mg based MNMs with excellent biocompatibility and harmless byproducts hold enormous potential for drug delivery applications.^[95] PEDOT/Zn micromotors represent the first in vivo application of synthetic MNMs for gastric drug delivery.^[94] The acid-driven Zn micromotors could self-propel and penetrate the stomach tissue for prolonged retention and localized release of the cargo. Mg/Pt-poly(N-isopropylacrylamide) (pNIPAM) Janus micromotors were autonomously propelled in simulated body fluids or blood plasma without any other additives.^[161] The temperature-responsive pNIPAM underwent a swelling and squeeze effect at low and physiological temperatures to load and release the payloads, respectively (Figure 8 F). The Mg micromotors can rapidly neutralize the acidity of the stomach fluid due to the depletion of protons by reaction with Mg.^[162] With a drug loaded, a pH responsive polymer coated onto the Mg particles can release the payload due to a pH change. Wang's group has reported Mg microparticle loaded PEDOT/Au microtubes coated with an enteric polymer for precise positioning, propulsion and retention in the mouse's gastrointestinal tract.^[163] The enteric polymer coating protected the micromotors from

reacting with the gastric acid, but dissolved in the intestinal fluid (pH 6-7) to trigger the propulsion for intestinal tissue penetration. By tailoring the thickness of the polymer coating, the dissolution time of the polymer could be tuned which in turn controlled the positioning of the motors inside the intestinal tract. Figure 8 G shows the illustrated mechanism of action and preparation scheme of PEDOT/Au/Mg micromotors coated with the enteric polymer. Due to the self-consumption of the material, Zn and Mg based micromotors offer unique opportunities for drug delivery due to their transient nature, which produces harmless byproducts and post-delivery separation is no longer needed.^[164] Kastrup *et al.* have used self-propelled CaCO_3 particles to transport therapeutics through blood.^[165] The particles were synthesized by controlled precipitation of CaCl_2 and Na_2CO_3 , and mixed with protonated Tranexamic acid, a drug to prevent excessive blood loss. When injected into the blood, the particles were propelled by releasing CO_2 for a distance of millimeters into the vasculature of wounds. Thrombin loaded particles worked as an efficient hemostatic agent.

Catalase based micromotors with encapsulated DOX were prepared by layer-by-layer assembly of polyelectrolytes.^[166,167] The micromotors navigated to the cancer cells and drug release was accomplished by exposure to the near-infrared (NIR) light to collapse the polyelectrolyte layers. MNMs driven by biofluids such as urea or glucose,^[129,130] hold a great promise for in vivo drug delivery applications, which yet remains to be demonstrated. Synthetic MNMs with immobilized urease offer another potential benefit besides actively driving the motion. The natural defense mechanism of the gastrointestinal and urinary tract contains mucin that is responsible for the mechanical properties of the mucosal lining and restricts the penetration of foreign substances. A stomach inhabiting bacteria *Helicobacter pylorus* manipulates the gastric mucus by releasing urease that locally neutralizes the pH by producing ammonia from urea. A change in the pH induces a sol-gel transition in the mucus to reduce its viscosity and allows the bacteria to penetrate through it.^[168] This provides a promise for synthetic MNMs to adopt a similar strategy for mucosal penetration by

immobilizing urease onto their external surface.^[169] The operational mechanism of *H. pylori* and urease-immobilized micropropellers is shown in Figure 8 H. Other proof-of-concept biomedical applications include micromotor-assisted immunoassays and immunosensing for protein and biomarker detection.^[155,170–173]

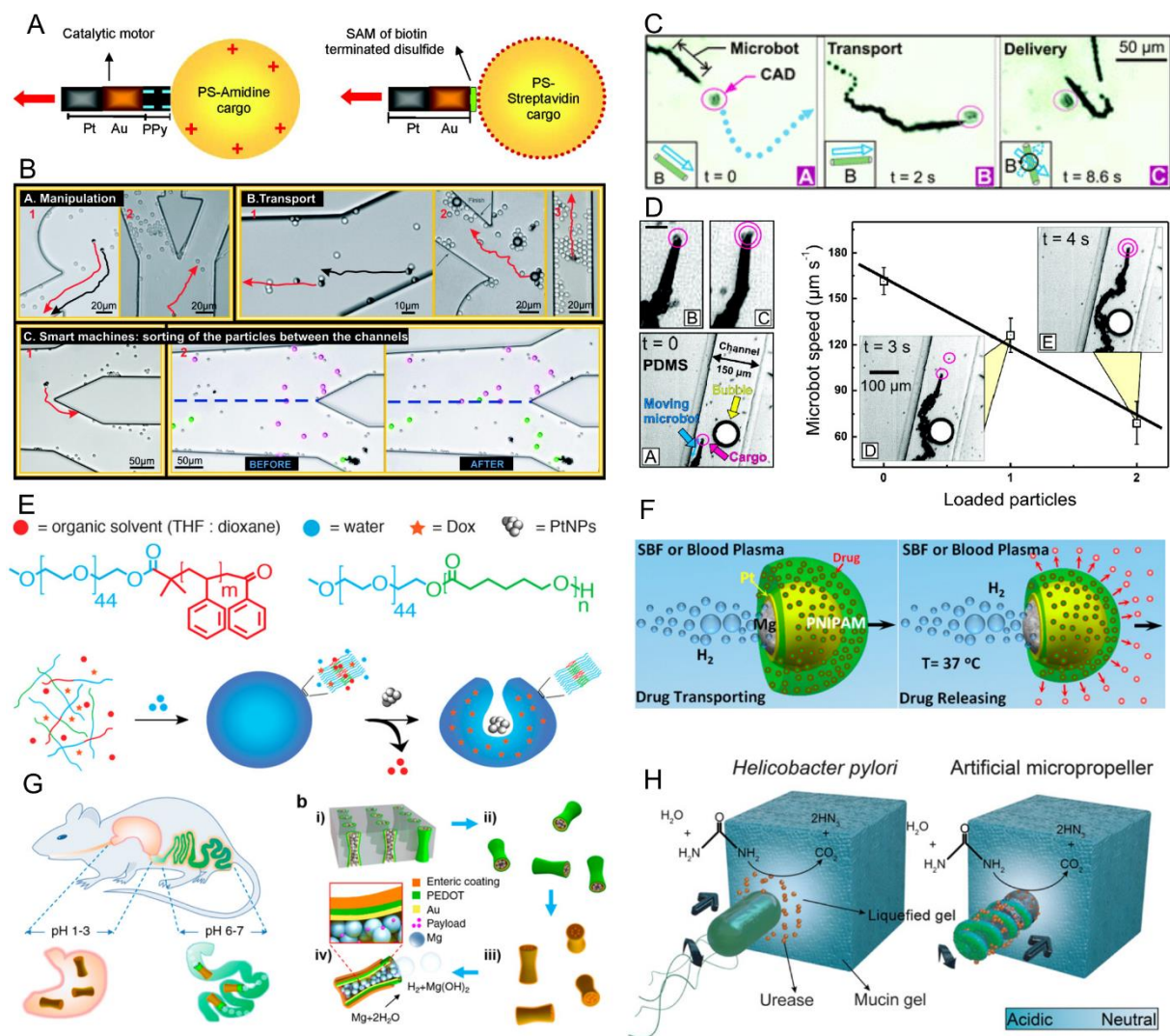


Figure 8. (A-D) Cargo towing applications.; (A) Cargo attachment to the nanorods by electrostatic interaction between the negative PPy end of a Pt-Au-PPy motor and a positively charged PS amidine microsphere (left), and biotin-streptavidin binding between the Au tips of Pt-Au rods functionalized with a biotin-terminated disulfide and streptavidin-coated cargo (right). Reproduced with permission.^[144] Copyright 2008, American Chemical Society. (B) manipulation of colloidal cargo in microfluidic channels using magnetic Pt/SiO₂ micromotors. Reproduced with permission.^[40] Copyright 2012, American Chemical Society. (C) manipulation of neuronal CAD cells (catecholaminergic cell line) by rolled-up Ti/Fe/Pt microtubes. Reproduced with permission.^[150] Copyright 2011, Royal Society of Chemistry.

(D) loading and transport of 5 μm PS cargo particles by the Ti/Fe/Pt micromotors in a microchannel. Reproduced with permission.^[149] Copyright 2011, American Chemical Society. (E-H) Drug delivery applications of the MNMs.; (E) Self-assembly of stomatocyte nanomotors loaded with DOX and Pt-NPs. Reproduced with permission.^[160] Copyright 2017, American Chemical Society. (F) Illustration of Mg based micromotor coated with drug loaded pNIPAM layer for drug delivery at physiological conditions. Reproduced with permission.^[161] Copyright 2014, American Chemical Society. (G) a) Schematic illustration of in vivo operation of the Mg based micromotors coated with an enteric polymer for propulsion and localized delivery to the GI tract; b) scheme of preparation: (i) loading of Mg microspheres and payload into PEDOT/Au microtubes electrodeposited in a PC membrane; (ii) dissolution of PC membrane and release the Mg micromotors; (iii) coating Mg micromotors with enteric polymer; (iv) dissolution of the enteric coating and propulsion of Mg micromotors in solution with neutral pH. Reproduced with permission.^[163] Copyright 2016, American Chemical Society. (H) Schematic illustration of the propulsion strategy of *Helicobacter pylori* and the enzymatically active micropropellers through mucin gels. The enzyme on the surface of the helices hydrolyzes urea and liquefies the environment via the resulting local rise in pH. Reproduced with permission.^[169] Copyright 2015, American Association for the Advancement of Science.

4.3. Environmental applications

A rapid increase in global industrialization has resulted in excessive disposal of toxic pollutants into the environment. This has posed a serious threat to the aquatic ecosystem, which is vital for humans. An interruption in the supply of clean water may affect millions of lives, which makes it a matter of great scientific, economic and political interest. Some examples of the toxic pollutants that are disposed-off by the industry are organic solvents, personal care or consumer products, pharmaceuticals, pesticides, heavy metal contaminants and miscellaneous excipients/additives used in various product formulations. Nanotechnology and nanomaterials present innovative technologies for sensing and removal of pollutants due to their excellent optical and catalytic properties, high surface area and tunable surface chemistry.^[174] The next generation of water remediation solutions aims at low-cost and energy

efficient approaches to remove biological and chemical pollutants, even at remote locations where conventional methods cannot be implemented. Chemically driven MNMs hold a unique promise for environmental remediation applications due to their superior catalytic properties and autonomous propulsion that can speed up the diffusion-limited processes. The environmental applications of MNMs include sensing and removal of the pollutants. Environmental sensing refers to the changes in the motion behavior of MNMs in the presence of certain contaminants. For example, Pt/Au bimetallic nanorods show dramatic acceleration in the presence of Ag^+ ions (Figure 9 A).^[13] The Ag^+ ions adsorb onto the Pt surface and are reduced in the presence of H_2O_2 into metallic Ag, which increases the electrocatalytic properties of the nanomotors for a faster motion. The motion enhancement is strongly dependent on the concentration of Ag^+ ions and can be used to obtain quantitative information of the Ag^+ toxicity down to the nanomolar level. In contrast, contaminants can also negatively influence the motion of MNMs by deactivating or poisoning the catalysts.^[175] Catalase based micromotors undergo drastic changes in their speeds in the presence of various inorganic and organic pollutants that inhibit the enzymatic activity, as illustrated in Figure 9 B.^[176] An analysis of common ecotoxicological parameters, such as the exposure concentration that causes 50% attenuation of micromotor motion (EC_{50}) and the lifetime expectancy, allows a direct real-time assessment of the water quality by optically tracking the motion behavior. A similar response of the motile micromotors to the vapor plumes of chemical warfare agents (CWAs) enables their rapid and convenient detection.^[177] The catalase-based micromotors remain active in the absence of CWAs, but once present, the CWA vapors inhibit the catalase activity and attenuate the motion. Fluorescent MNMs can detect the presence of certain organic or inorganic pollutants that quench the fluorescence intensity in contaminated water.^[178,179] Micromotor-assisted fluid mixing and accelerated chemical degradation of OP threats also allow for rapid electrochemical monitoring of the decontamination processes.^[180] Rapid conversion of the non-detectable paraoxon into electroactive p-nitrophenol can be

monitored using printed electrochemical sensor strips. The mechanism and reactions involved are shown in Figure 9 C.

Guix et al. reported the first example of using synthetic MNMs for environmental remediation.^[181] The outer surface of the Au sputtered, Pt based microtubes was functionalized with alkanethiols for the capture and removal of oil microdroplets as a possible solution to oil spillage. However, due to a similar affinity of thiol groups for Pt and Au, the Pt catalytic surface was deactivated and the propulsion efficiency was severely reduced. We have recently proposed the use of MnO₂ deposited onto the Pt surface to block the microtube opening, which protects the Pt surface from the chemisorption of thiol compounds.^[182] The resulting micromotors maintained excellent performance after alkanethiol functionalization and were used for the capture and transport of oil droplets. The oil capture and removal by hydrophobic Mn and Mg based micromotors have also been reported.^[87,96]

Non-biogenic organic dyestuff released by the paints, textile and printing industry is another problem that requires innovative solutions for their degradation or recovery. Rolled-up Fe/Pt microtubes were used for Fenton-like degradation of dye molecules.^[183,184] Figure 9 D illustrates the degradation process of rhodamine 6G. The micromotors could continuously move over 24 hours and were reusable for multiple cleaning cycles over a period of several weeks. Wani et al. described a dual effect of the MnO₂ microparticles which provided efficient catalytic degradation and adsorptive bubble separation of rhodamine 6G and methylene blue dyes as depicted in Figure 9 E.^[185] These particles were obtained commercially and could undergo motion for a few hours, which was followed by self-degradation. The low cost, the easy availability of MnO₂ in bulk quantities and the transient nature of commercial MnO₂ microparticles makes them an attractive choice for practical water remediation applications. Besides dyes, other highly stable organic ingredients used in plastics, electronics, furniture, cosmetics and personal care products may be released into the environment. The hydrophobic nature of reduced graphene oxide (rGOx) is known to adsorb

organic compounds through π - π stacking interactions.^[186] SiO₂ particles wrapped with rGOx nanosheets and a Pt hemisphere can dynamically and efficiently remove polybrominated diphenyl ethers and triclosan from environmental samples.^[187]

Increasing concentrations of toxic heavy metals in the soil and aquatic ecosystem also requires strict measures on their release and efficient methods for their removal. GOx nanosheets can adsorb heavy metal ions due to the complexation between the oxygen moieties of the nanosheets and the metal ions. Self-propelling micromotors comprising an outer GOx layers could capture and remove lead (Pb²⁺) ions from the contaminated waters 10 times more efficiently than their nonmotile counterparts.^[188] Another efficient approach for the removal of heavy metal contaminations is to use metal chelating agents that can be easily functionalized on the surface of MNMs. Wang's group used Au/Ti/Mg Janus particles functionalized with meso-2,3-dimercaptosuccinic acid (DMSA) for the removal of Zn²⁺, Cd²⁺ and Pb²⁺ ions from contaminated water.^[189] These micromotors were driven by water and did not require any external fuel, having a lifetime of ~3 minutes. A metal removal efficiency of up to 100% was observed after just 2 min of operation. Such a straightforward approach can be extended to different chelating agents to address specific cleanup needs.

In the defense industry, the conversion of chemical warfare agents into non-toxic products at the remote storage locations is another big challenge that relies on peroxide based oxidative treatment. However, the prolonged processing times and the need for mechanical mixing to enhance the mass transfer are some of the undesired conditions that are difficult to fulfil in remote locations. Bubble-propelled Pt based micromotors have shown a remarkable increase in the oxidative decontamination of organophosphate (OP) nerve agents by generating peroxide anions (OOH⁻) *in situ*, without any external agitation.^[111] Water-driven Mg-based micromotors can also photocatalytically decontaminate water samples poisoned with chemical and biological contaminants, such as OP nerve agents and anthrax stimulant *Bacillus globigii* spore.^[190] A modification of the micromotors with bactericidal materials

such as chitosan has a potential to clean water from pathogenic bacteria.^[191] The antibacterial activity of chitosan can be attributed to an electrostatic interaction with the cell membrane and its consequent damage.

Besides chemical degradation, self-propelling platforms can remove organic and inorganic pollutants from contaminated water by processes based on adsorption or selective binding.^[192-194] Carbon dioxide (CO₂) emission into the atmosphere is another major threat to the environment and a central cause for the climate change. Current CO₂ capture and sequestration methods suffer either from the high cost, the high energy input or the use of hazardous chemicals that may further pollute the environment.^[195] Uygun et al. used carbonic anhydrase (CA) immobilized microtubes for biocatalytic sequestration of CO₂.^[196] The enzyme-catalyzed hydration of CO₂ and conversion into CaCO₃ by the self-propelling micromotors is a promising development towards mobile microsystems for CO₂ sequestration.

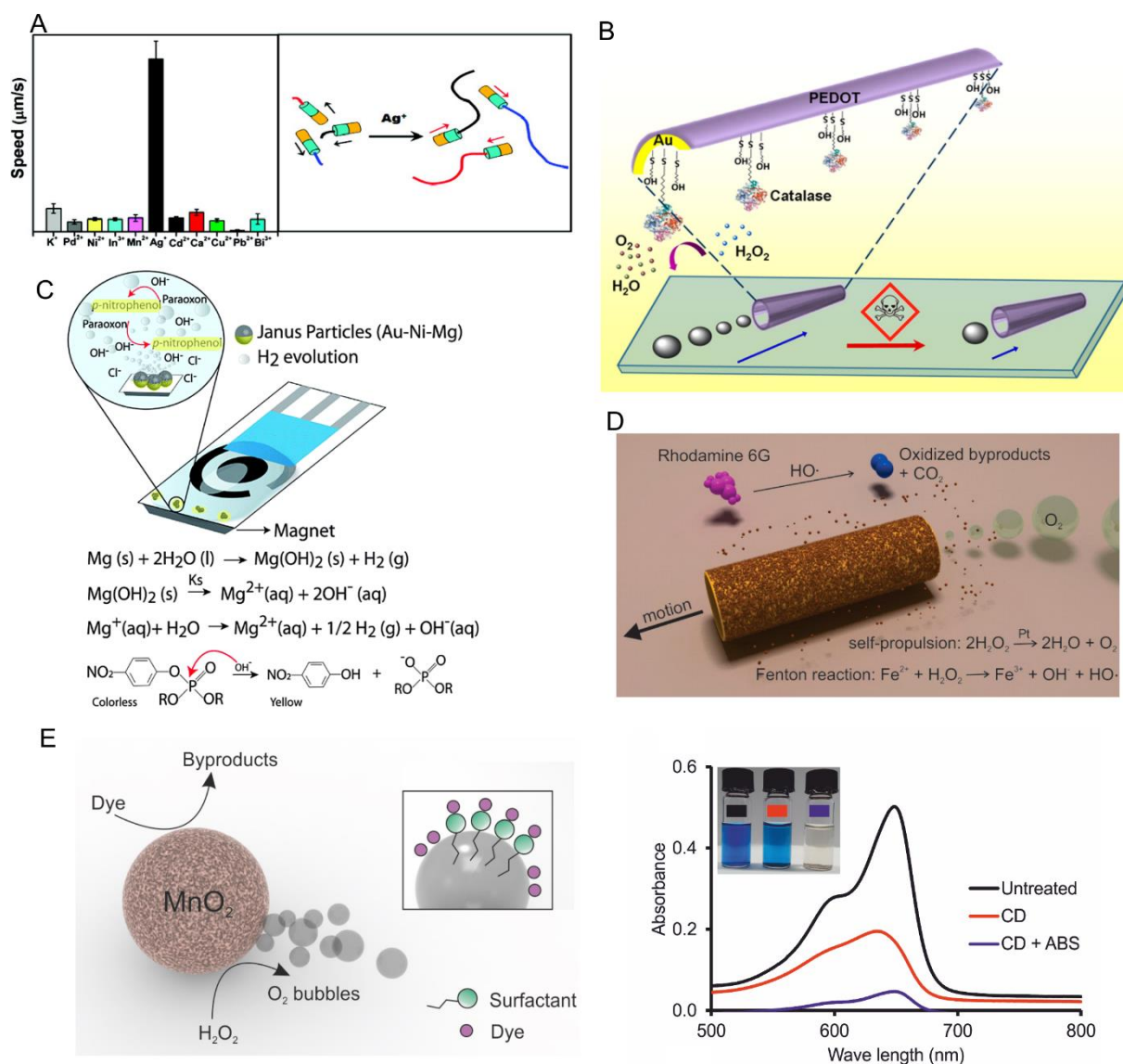


Figure 9. Environmental applications of chemically driven MNMs. (A) Motion of Pt/Au nanorods in the presence of 100 μM metal-nitrate salt solution of different metals, in 5% H_2O_2 . The speed enhancement in the presence of Ag^+ ions provides a route to determine the aquatic Ag^+ toxicity. Reproduced with permission.^[13] Copyright 2010, American Chemical Society. (B) Catalase immobilized tubular motors (top), and the effect of pollutants on the locomotion speed due to the inhibition of catalase (bottom). Reproduced with permission.^[176] Copyright 2013, American Chemical Society. (C) The operation of printed electrochemical sensor strip in the presence of Mg micromotors and the reactions involved in the degradation of paraoxon into p-nitrophenol. Reproduced with permission.^[180] Copyright 2015, Royal Society of Chemistry. (D) Conversion of an organic dye into byproducts due to a Fenton-like reaction by the Fe/Pt tubular motors. Reproduced with permission.^[183] Copyright 2013, American Chemical Society. (E) Illustration of the dual effect of MnO_2 micromotors in the wastewater treatment. The reactive (radical) species generated during the decomposition of

H_2O_2 degrades the dye molecules. The bubbles formed in the presence of a surfactant adsorb the dye molecules and form foam at the top of the dye solution via a process known as adsorptive bubble separation, for subsequent recovery (left). Light absorption spectra of methylene blue, prior and after catalytic degradation (CD) without and with adsorptive bubble separation (ABS). The inset shows the respective images of the solutions before and after the treatment. Reproduced with permission.^[185] Copyright 2016, Wiley-VCH.

4.4. Other applications

MNMs have been utilized in several other interesting applications, which do not fall under the categories as described above, and will be summarized here. Singh et al. used Janus Pt-black/Ti particles to self-propel and produce H_2 gas for energy applications.^[197] The large catalytic surface of Pt-black particles produced H_2 at a much faster rate that could drive a hydrogen-oxygen fuel cell based model car by producing H_2 and O_2 gases using sodium borohydride (NaBH_4) and H_2O_2 fuels. Figure 10 A presents the photograph of the model car setup and scheme of the hydrogen-oxygen fuel cell. The self-healing ability of biological organisms has inspired researchers to employ micromotors to search and localize at the microscopic cracks for repairing microelectronic circuits.^[198] The repair mechanism relies on the localization of motile Pt/Au microparticles at the surface cracks of broken circuits to bridge the flow of electrons. The operational mechanism is illustrated in Figure 10 B. A new concept of self-propelled supercapacitors is introduced by Pumera's group that involves WS_2 NPs-PANI/Pt microtubes.^[199] The supercapacitor microdevices trapped by the Au electrodes integrated in microfluidic channels exhibit superior specific capacitance for on-demand manipulation of electronic devices.

Limited resolution of optical microscopy techniques has drawn interest to design new materials and microlenses for visualizing features below the diffraction limit.^[200,201] However, the integrated microlenses do not allow site-specific inspection of the surfaces. Self-propelled spherical micromotors comprising of a high-refractive index material may function as mobile

microlenses to scan over larger areas. Polystyrene microspheres partially coated with Ni and Pt layers can be guided in a controlled manner for point-to-point nanoscopic imaging.^[202] In Figure 10 C, a schematic of the operation of micromotor-based nanoscopic imaging platform is shown.

Nanomotor lithography has been described as a new nano-patterning approach to fabricate submicron and nanometer scale features.^[203] The opaque metallic nanorods function as nanoscale masks while the transparency of Janus spheres allows near-field concentration of the light, to pattern a photoresist layer. Depending upon the use of nanorods or Janus spheres for patterning, a raised ridge or a trench line can be obtained.

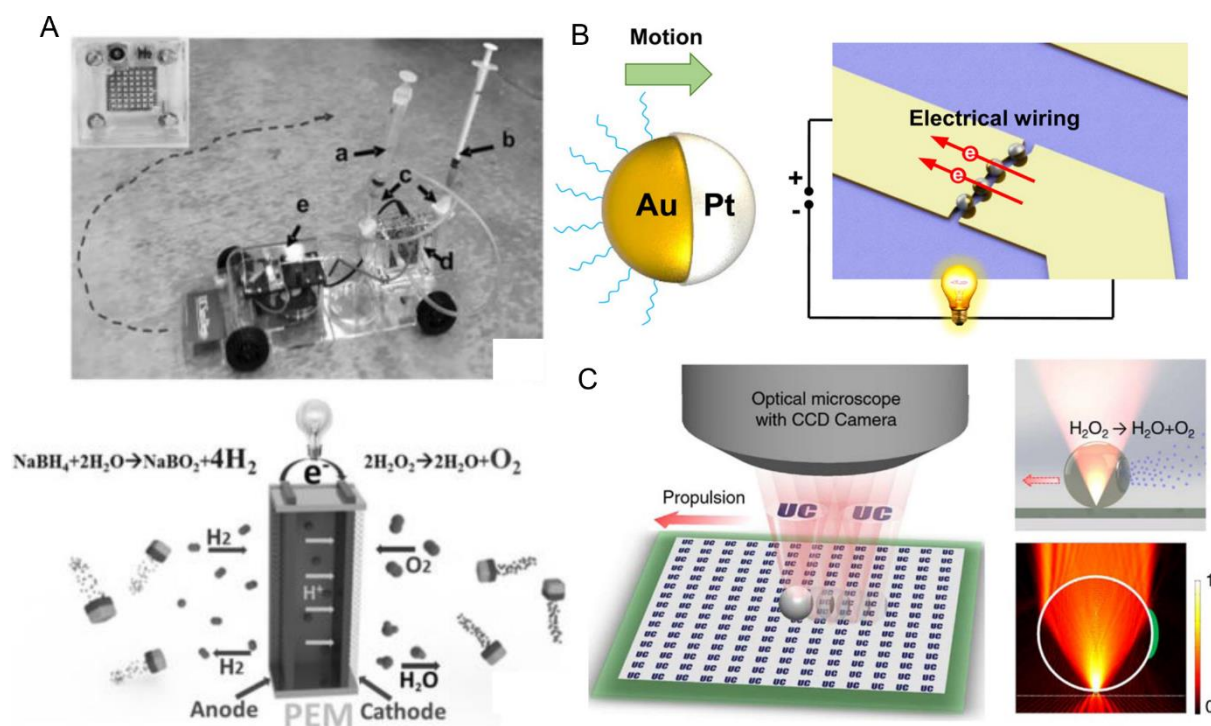


Figure 10. (A) (top) The model car driven by fuel cell which operates by the production of H_2 and O_2 using NaBH_4 and H_2O_2 , respectively; a) NaBH_4 reservoir, b) H_2O_2 reservoir, c) Pt-black/Ti particles, d) motor-based hydrogen–oxygen fuel cell (also shown in inset), and e) electric motor.; (bottom) schematic of the hydrogen–oxygen fuel cell based on co-generation of H_2 and O_2 . Reproduced with permission.^[197] Copyright 2015, Wiley-VCH. (B) Schematic view of the repair process of a broken electronic circuit by Pt/Au nanomotors to restore conductivity. The nanomotors self-propel and are trapped by the cracks to bridge the voids. Reproduced with permission.^[198] Copyright 2015, American Chemical Society. (C)

Micromotor assisted optical nanoscopy; illustration of motion based imaging by the high-refractive index microsphere lens.; chemically powered propulsion and light amplification by the microsphere lens., finite element model of a point light source passing through 10 μm microsphere lens ($n = 1.59$) in water ($n = 1.33$). The catalytic segment is shown in green. Reproduced with permission.^[202] Copyright 2016, American Chemical Society.

5. Summary and outlook

In this report, we provided a summary of the progress towards chemically driven MNMs. Pt is the most widely used material for the fabrication of catalytic MNMs. The non-toxicity, excellent catalytic activity and availability of different fabrication methods makes Pt a potential candidate to prepare MNMs of distinct geometrical designs, such as tubes, rods and Janus spheres. Another attractive feature of Pt based MNMs is their prolonged operation lifetime. Pt is an inert material that does not degrade during the decomposition of H_2O_2 , so motion lasts unless the fuel is consumed. A replenishment of the fuel reinitiates the motion. However, Pt is a very expensive trace element and is not available in large quantities essentially required for practical environmental applications. Micromotors based on Ag and MnO_2 are also functional in a way similar to Pt. However, the aquatic toxicity of Ag is a major concern that restricts its practical use. Mn_yO_x is an intriguing alternate material to Pt and Ag, but the design of MnO_2 based MNMs requires the synthesized crystalline form to be considered, since it determines the propulsion efficiency as well as the operational lifetime of the particles. Ni, Ir, Ru, Pd and MOFs are potential alternates but of a relatively inferior catalytic efficiency. A common limitation of the aforementioned materials is the required use of toxic chemicals (hydrazine or H_2O_2) as fuels. The bio-incompatibility of such fuels restricts their use in biomedical applications. Nevertheless, these materials hold a significant promise for environmental remediation applications because the reaction by-products are non-toxic.

Micromotors that are based on Mg and Zn can be propelled by their reaction with water and acids to produce H₂ gas bubbles. Both Zn and Mg based micromotors have demonstrated their potential for *in vivo* biomedical applications. Other materials that have been explored for MNMs include Al/Pd and Al-Ga alloys, CaCO₃, and Fe. Enzymes have been used to substitute inorganic catalysts in MNMs, but their lifetime strongly depends upon the chemical environment. Some solution conditions used for MNMs may inhibit or completely inactivate the enzymatic activity. So far, urease and glucose oxidase have been used to prepare enzyme-driven MNMs, propelled by biological fuels, i.e., urea and glucose, respectively.

A variety of proof-of-concept applications of MNMs have been presented, such as cargo towing, immunoassays, drug delivery, environmental sensing and remediation, as well as energy production and storage. This suggests a great potential for self-propelled MNMs in the future to solve some technical challenges of the conventional drug delivery and environmental remediation applications. In the meanwhile, the efforts should be directed to the exploration of novel, efficient and environmentally friendly materials that could utilize less toxic or even completely non-toxic, biologically relevant fuels. It remains to be seen how the enzyme-driven nanomotors will respond in viscous environments (e.g. a circulating blood stream), in order to assess their feasibility for practical biomedical applications.

Despite the huge progress in the field, there are no large or industrial scale applications of MNMs yet reported. Thus, a research focus should be broadened to include studies beyond the proof-of-concept level. In the perspective of environmental applications, any undesired effects of the MNMs to the environment after accomplishing a remediation process should also be considered. The MNMs that could self-degrade into harmless products, after completing a process in a certain period of time, would be highly advantageous. Otherwise, scalable methods for the isolation of MNMs need to be devised.

Acknowledgements

MS acknowledges the financial support provided by the Faculty of Science and Forestry, University of Eastern Finland.

Received: ((will be filled in by the editorial staff))
Revised: ((will be filled in by the editorial staff))
Published online: ((will be filled in by the editorial staff))

References

- [1] R. D. Vale, R. a Milligan, *Science* **2000**, 288, 88.
- [2] M. K. J. Ter Wiel, R. A. Van Delden, A. Meetsma, B. L. Feringa, *J. Am. Chem. Soc.* **2003**, 125, 15076.
- [3] Y. Amatatsu, *Bull. Chem. Soc. Jpn.* **2015**, 88, 1417.
- [4] M. R. Wilson, J. Solà, A. Carlone, S. M. Goldup, N. Lebrasseur, D. A. Leigh, *Nature* **2016**, 534, 235.
- [5] J. D. Badjic, V. Balzani, A. Credi, S. Silvi, J. F. Stoddart, *Science (80-.)*. **2004**, 303, 1845.
- [6] K. Ariga, J. Li, J. Fei, Q. Ji, J. P. Hill, *Adv. Mater.* **2016**, 28, 1251.
- [7] S. Kassem, T. van Leeuwen, A. S. Lubbe, M. R. Wilson, B. L. Feringa, D. A. Leigh, *Chem. Soc. Rev.* **2017**, 46, 2592.
- [8] T. Xu, W. Gao, L. P. Xu, X. Zhang, S. Wang, *Adv. Mater.* **2017**, 29, 1603250.
- [9] K. J. Rao, F. Li, L. Meng, H. Zheng, F. Cai, W. Wang, *Small* **2015**, 11, 2836.
- [10] J. Li, B. Esteban-Fernández de Ávila, W. Gao, L. Zhang, J. Wang, *Sci. Robot.* **2017**, 2, eaam6431.
- [11] J. Orozco, G. Cheng, D. Vilela, S. Sattayasamitsathit, R. Vazquez-Duhalt, G. Valdés-Ramírez, O. S. Pak, A. Escarpa, C. Kan, J. Wang, *Angew. Chem. Int. Ed.* **2013**, 52,

13276.

- [12] J. Wang, *Lab Chip* **2012**, *12*, 1944.
- [13] D. Kagan, P. Calvo-marzal, S. Balasubramanian, K. M. Manesh, G. Flechsig, J. Wang, *J. Am. Chem. Soc.* **2010**, *131*, 12082.
- [14] J. Hu, S. Zhou, Y. Sun, X. Fang, L. Wu, *Chem. Soc. Rev.* **2012**, *41*, 4356.
- [15] A. Walther, A. H. E. Müller, *Chem. Rev.* **2013**, *113*, 5194.
- [16] J. R. Howse, R. A. L. Jones, A. J. Ryan, T. Gough, R. Vafabakhsh, R. Golestanian, *Phys. Rev. Lett.* **2007**, *99*, 48102.
- [17] S. Ebbens, D. A. Gregory, G. Dunderdale, J. R. Howse, Y. Ibrahim, T. B. Liverpool, R. Golestanian, *Europhys. Lett.* **2014**, *106*, 58003.
- [18] A. T. Brown, W. C. K. Poon, *Soft Matter* **2014**, *10*, 4016.
- [19] M. Ibele, T. E. Mallouk, A. Sen, *Angew. Chem. Int. Ed.* **2009**, *48*, 3308.
- [20] M. E. Ibele, P. E. Lammert, V. H. Crespi, A. Sen, *ACS Nano* **2010**, *4*, 4845.
- [21] W. F. Paxton, A. Sen, T. E. Mallouk, *Chem. Eur. J.* **2005**, *11*, 6462.
- [22] S. Sanchez, L. Soler, J. Katuri, *Angew. Chem. Int. Ed.* **2015**, *54*, 1414.
- [23] H. Wang, M. Pumera, *Chem. Rev.* **2015**, *115*, 8704.
- [24] R. F. Ismagilov, A. Schwartz, N. Bowden, G. M. Whitesides, *Angew. Chem. Int. Ed.* **2002**, *41*, 652.
- [25] W. F. Paxton, K. C. Kistler, C. C. Olmeda, A. Sen, S. K. St Angelo, Y. Y. Cao, T. E. Mallouk, P. E. Lammert, V. H. Crespi, *J. Am. Chem. Soc.* **2004**, *126*, 13424.
- [26] W. F. Paxton, P. T. Baker, T. R. Kline, Y. Wang, T. E. Mallouk, A. Sen, *J. Am. Chem. Soc.* **2006**, *128*, 14881.
- [27] Y. Wang, R. M. Hernandez, D. J. Bartlett, J. M. Bingham, T. R. Kline, A. Sen, T. E. Mallouk, *Langmuir* **2006**, *22*, 10451.
- [28] T. R. Kline, W. F. Paxton, T. E. Mallouk, A. Sen, *Angew. Chem. Int. Ed.* **2005**, *44*, 744.

- [29] R. Laocharoensuk, J. Burdick, J. Wang, *ACS Nano* **2008**, *2*, 1069.
- [30] U. K. Demirok, R. Laocharoensuk, K. M. Manesh, J. Wang, *Angew. Chem. Int. Ed.* **2008**, *47*, 9349.
- [31] L. Qin, M. J. Banholzer, X. Xu, L. Huang, C. A. Mirkin, *J. Am. Chem. Soc.* **2007**, *129*, 14870.
- [32] Y. Wang, S. T. Fei, Y. M. Byun, P. E. Lammert, V. H. Crespi, A. Sen, T. E. Mallouk, *J. Am. Chem. Soc.* **2009**, *131*, 9926.
- [33] S. Balasubramanian, D. Kagan, K. M. Manesh, P. Calvo-Marzal, G. U. Flechsig, J. Wang, *Small* **2009**, *5*, 1569.
- [34] P. Calvo-Marzal, K. M. Manesh, D. Kagan, S. Balasubramanian, M. Cardona, G.-U. Flechsig, J. Posner, J. Wang, *Chem. Commun.* **2009**, 4509.
- [35] G. Loget, A. Kuhn, *J. Mater. Chem.* **2012**, *22*, 15457.
- [36] R. Golestanian, T. B. Liverpool, A. Ajdari, *Phys. Rev. Lett.* **2005**, *94*, 1.
- [37] H. Ke, S. Ye, R. L. Carroll, K. Showalter, *J. Phys. Chem. A* **2010**, *114*, 5462.
- [38] L. F. Valadares, Y. G. Tao, N. S. Zacharia, V. Kitaev, F. Galembeck, R. Kapral, G. a. Ozin, *Small* **2010**, *6*, 565.
- [39] J. G. Gibbs, N. A. Fragnito, Y. Zhao, *Appl. Phys. Lett.* **2010**, *97*, 1.
- [40] L. Baraban, D. Makarov, R. Streubel, I. Mönch, D. Grimm, S. Sanchez, O. G. Schmidt, *ACS Nano* **2012**, *6*, 3383.
- [41] L. Baraban, D. Makarov, O. G. Schmidt, G. Cuniberti, P. Leiderer, A. Erbe, *Nanoscale* **2013**, *5*, 1332.
- [42] J. Simmchen, J. Katuri, W. E. Uspal, M. N. Popescu, M. Tasinkevych, S. Sánchez, *Nat. Commun.* **2016**, *7*, 10598.
- [43] L. Baraban, S. M. Harazim, S. Sanchez, O. G. Schmidt, *Angew. Chem. Int. Ed.* **2013**, *52*, 5552.
- [44] N. H. Fletcher, *J. Chem. Phys.* **1958**, *29*, 572.

- [45] M. Manjare, B. Yang, Y. P. Zhao, *Phys Rev Lett* **2012**, *109*, 128305.
- [46] S. Wang, N. Wu, *Langmuir* **2014**, *30*, 3477.
- [47] W. Gao, M. Liu, L. Liu, H. Zhang, B. Dong, C. Y. Li, *Nanoscale* **2015**, *7*, 13918.
- [48] U. Choudhury, L. Soler, J. G. Gibbs, S. Sanchez, P. Fischer, *Chem. Commun.* **2015**, *51*, 8660.
- [49] X. Ma, J. Katuri, Y. Zeng, Y. Zhao, S. Sanchez, *Small* **2015**, *11*, 5023.
- [50] X. Ma, S. Jang, M. N. Popescu, W. E. Uspal, A. Miguel-Lopez, K. Hahn, D. P. Kim, S. Sanchez, *ACS Nano* **2016**, *10*, 8751.
- [51] D. A. Wilson, R. J. M. Nolte, J. C. M. van Hest, *Nat. Chem.* **2012**, *4*, 268.
- [52] Y. Tu, F. Peng, X. Sui, Y. Men, P. B. White, J. C. M. van Hest, D. A. Wilson, J. C. M. van Hest, D. A. Wilson, *Nat. Chem.* **2016**, *9*, 480.
- [53] S. Sengupta, K. K. Dey, H. S. Muddana, T. Tabouillot, M. E. Ibele, P. J. Butler, A. Sen, *J. Am. Chem. Soc.* **2013**, *135*, 1406.
- [54] T. C. Lee, M. Alarcón-Correa, C. Miksch, K. Hahn, J. G. Gibbs, P. Fischer, *Nano Lett.* **2014**, *14*, 2407.
- [55] D. Yi, Q. Zhang, Y. Liu, J. Song, Y. Tang, F. Caruso, Y. Wang, *Angew. Chem. Int. Ed.* **2016**, *55*, 14733.
- [56] A. A. Solovev, Y. F. Mei, E. B. Urena, G. S. Huang, O. G. Schmidt, *Small* **2009**, *5*, 1688.
- [57] K. M. Manesh, M. Cardona, R. Yuan, M. Clark, D. Kagan, S. Balasubramanian, J. Wang, *ACS Nano* **2010**, *4*, 1799.
- [58] G. Zhao, A. Ambrosi, M. Pumera, *J. Mater. Chem. A* **2014**, *2*, 1219.
- [59] H. Wang, J. G. S. Moo, M. Pumera, *Nanoscale* **2014**, *6*, 11359.
- [60] K. Yao, M. Manjare, C. A. Barrett, B. Yang, T. T. Salguero, Y. Zhao, *J. Phys. Chem. Lett.* **2012**, *3*, 2204.
- [61] W. Gao, S. Sattayasamitsathit, J. Orozco, J. Wang, *J. Am. Chem. Soc.* **2011**, *133*,

- 11862.
- [62] W. Gao, S. Sattayasamitsathit, A. Uygun, A. Pei, A. Ponedal, J. Wang, *Nanoscale* **2012**, *4*, 2447.
- [63] A. Martín, B. Jurado-Sanchez, A. Escarpa, J. Wang, *Small* **2015**, *11*, 3568.
- [64] V. V. Singh, K. Kaufmann, B. E. F. de Ávila, E. Karshalev, J. Wang, *Adv. Funct. Mater.* **2016**, *26*, 6270.
- [65] R. Maria-Hormigos, B. Jurado-Sanchez, L. Vazquez, A. Escarpa, *Chem. Mater.* **2016**, *28*, 8962.
- [66] Z. Wu, Y. Wu, W. He, X. Lin, J. Sun, Q. He, *Angew. Chem. Int. Ed.* **2013**, *52*, 7000.
- [67] A. A. Solovev, E. J. Smith, C. C. B. Bufon, S. Sanchez, O. G. Schmidt, *Angew. Chem. Int. Ed.* **2011**, *50*, 10875.
- [68] S. Sanchez, A. N. Ananth, V. M. Fomin, M. Viehrig, O. G. Schmidt, *J. Am. Chem. Soc.* **2011**, *133*, 14860.
- [69] H. Wang, G. J. Zhao, M. Pumera, *J. Phys. Chem. C* **2014**, *118*, 5268.
- [70] W. J. Huang, M. Manjare, Y. P. Zhao, *J. Phys. Chem. C* **2013**, *117*, 21590.
- [71] G. Zhao, M. Pumera, *Nanoscale* **2014**, *6*, 11177.
- [72] M. Safdar, T. Itkonen, J. Janis, *RSC Adv.* **2015**, *5*, 13171.
- [73] G. J. Zhao, M. Viehrig, M. Pumera, *Lab Chip* **2013**, *13*, 1930.
- [74] H. Wang, G. J. Zhao, M. Pumera, *Phys. Chem. Chem. Phys.* **2013**, *15*, 17277.
- [75] Y. Mei, G. Huang, A. A. Solovev, E. B. Ureña, I. Mönch, F. Ding, T. Reindl, R. K. Y. Fu, P. K. Chu, O. G. Schmidt, *Adv. Mater.* **2008**, *20*, 4085.
- [76] H. Wang, G. Zhao, M. Pumera, *J. Am. Chem. Soc.* **2014**, *136*, 2719.
- [77] C. Huang, X. Shen, *Chem. Commun. (Camb)*. **2014**, *50*, 2646.
- [78] M. Liu, L. Liu, W. Gao, M. Su, Y. Ge, L. Shi, H. Zhang, B. Dong, C. Y. Li, *Nanoscale* **2014**, *6*, 8601.
- [79] W. Z. Teo, H. Wang, M. Pumera, *Chem. Commun.* **2016**, *52*, 4333.

- [80] V. V. Singh, B. Jurado-Sánchez, S. Sattayasamitsathit, J. Orozco, J. Li, M. Galarnyk, Y. Fedorak, J. Wang, *Adv. Funct. Mater.* **2015**, *25*, 2147.
- [81] W. Duan, M. Ibele, R. Liu, A. Sena, *Eur. Phys. J. E* **2012**, *35*, 77.
- [82] W. Duan, R. Liu, A. Sen, *J. Am. Chem. Soc.* **2013**, *135*, 1280.
- [83] F. Wong, A. Sen, *ACS Nano* **2016**, *10*, 7172.
- [84] X. Chen, G. Wu, T. Lan, W. Chen, *Chem. Commun.* **2014**, *50*, 7157.
- [85] X. Feng, Y. Zhang, Y. Li, Z. Huang, S. Chen, Y. Ma, L. Zhang, L. Wang, X. Yan, *Chem. Lett.* **2015**, *44*, 399.
- [86] A. K. Singh, T. K. Mandal, D. Bandyopadhyay, *RSC Adv.* **2015**, *5*, 64444.
- [87] F. Mou, D. Pan, C. Chen, Y. Gao, L. Xu, J. Guan, *Adv. Funct. Mater.* **2015**, *25*, 6173.
- [88] M. Safdar, O. M. Wani, J. Jänis, *ACS Appl. Mater. Interfaces* **2015**, *7*, 25580.
- [89] M. Safdar, T. Do Minh, N. Kinnunen, J. Janis, *ACS Appl. Mater. Interfaces* **2016**, *8*, 32624.
- [90] L. Wang, J. Chen, X. Feng, W. Zeng, R. Liu, X. L. Xiuqing Lin, Y. Ma, L. Wang, *RSC Adv.* **2016**, *6*, 65624.
- [91] H. H. Funke, H. Diaz, X. Liang, C. S. Carney, A. W. Weimer, P. Li, *Int. J. Hydrogen Energy* **2008**, *33*, 1127.
- [92] W. Gao, A. Uygun, J. Wang, *J. Am. Chem. Soc.* **2012**, *134*, 897.
- [93] S. Sattayasamitsathit, H. Kou, W. Gao, W. Thavarajah, K. Kaufmann, L. Zhang, J. Wang, *Small* **2014**, *10*, 2830.
- [94] W. Gao, R. Dong, S. Thamphiwatana, J. Li, W. Gao, L. Zhang, J. Wang, *ACS Nano* **2014**, *9*, 117.
- [95] F. Mou, C. Chen, H. Ma, Y. Yin, Q. Wu, J. Guan, *Angew. Chem. Int. Ed.* **2013**, *52*, 7208.
- [96] W. Gao, X. Feng, A. Pei, Y. Gu, J. Li, J. Wang, *Nanoscale* **2013**, *5*, 4696.
- [97] S. S. Fournier-Bidoz, A. C. A. C. Arsenault, I. Manners, G. A. Ozin, *Chem. Commun.*

- 2005, 4, 441.
- [98] J. Li, Q. Xiao, J.-Z. Jiang, G.-N. Chen, J.-J. Sun, *RSC Adv.* **2014**, 4, 27522.
- [99] W. Gao, A. Pei, R. Dong, J. Wang, *J. Am. Chem. Soc.* **2014**, 136, 2276.
- [100] W. Gao, A. Pei, J. Wang, *ACS Nano* **2012**, 6, 8432.
- [101] W. Gao, M. D'Agostino, V. Garcia-Gradilla, J. Orozco, J. Wang, *Small* **2013**, 9, 467.
- [102] W. Wang, W. Duan, Z. Zhang, M. Sun, A. Sen, T. E. Mallouk, *Chem. Commun.* **2015**, 51, 1020.
- [103] W. Wang, T. Y. Chiang, D. Velegol, T. E. Mallouk, *J. Am. Chem. Soc.* **2013**, 135, 10557.
- [104] E. L. Jewell, W. Wang, T. E. Mallouk, *Soft Matter* **2016**, 12, 2501.
- [105] L. L. del Mercato, M. Carraro, A. Zizzari, M. Bianco, R. Miglietta, V. Arima, I. Viola, C. Nobile, A. Sorarù, D. Vilona, G. Gigli, M. Bonchio, R. Rinaldi, *Chem. Eur. J.* **2014**, 20, 10910.
- [106] H. Furukawa, K. E. Cordova, M. O'Keeffe, O. M. Yaghi, *Science* **2013**, 341, 1230444.
- [107] T. T. Y. Tan, J. T. M. Cham, M. R. Reithofer, T. S. Andy Hor, J. M. Chin, *Chem. Commun.* **2014**, 50, 15175.
- [108] J. Li, X. Yu, M. Xu, W. Liu, E. Sandraz, H. Lan, J. Wang, S. M. Cohen, *J. Am. Chem. Soc.* **2017**, 139, 611.
- [109] W. Z. Teo, R. Zboril, I. Medrik, M. Pumera, *Chem. Eur. J.* **2016**, 22, 4789.
- [110] E. Karshalev, C. Chen, G. Marolt, A. Martín, I. Campos, R. Castillo, T. Wu, J. Wang, *Small* **2017**, 13, 1700035.
- [111] J. G. S. Moo, H. Wang, M. Pumera, *Chem. Commun.* **2014**, 50, 15849.
- [112] M. Guix, A. K. Meyer, B. Koch, O. G. Schmidt, *Sci. Rep.* **2016**, 6, 21701.
- [113] J. Vicario, R. Eelkema, W. R. Browne, A. Meetsma, R. M. La Crois, B. L. Feringa, *Chem. Comms.* **2005**, 3936.
- [114] S. Sanchez, A. A. Solovev, Y. Mei, O. G. Schmidt, *J. Am. Chem. Soc.* **2010**, 132,

- 13144.
- [115] J. Simmchen, A. Baeza, D. Ruiz, M. J. Esplandiu, M. Vallet-Regí, *Small* **2012**, *8*, 2053.
- [116] X. Ma, S. Sanchez, *Chem. Commun.* **2015**, *51*, 5467.
- [117] J. Simmchen, A. Baeza, D. Ruiz-Molina, M. Vallet-Regí, *Nanoscale* **2014**, *6*, 8907.
- [118] R. A. Larson, *Phytochemistry* **1988**, *27*, 969.
- [119] Y. Gu, S. Sattayasamitsathit, K. Kaufmann, R. Vazquez-Duhalt, W. Gao, C. Wang, J. Wang, *Chem. Commun.* **2013**, *49*, 7307.
- [120] S. Sattayasamitsathit, K. Kaufmann, M. Galarnyk, R. Vazquez-Duhalt, J. Wang, *RSC Adv.* **2014**, *4*, 27565.
- [121] H. S. Muddana, S. Sengupta, T. E. Mallouk, A. Sen, P. J. Butler, *J. Am. Chem. Soc.* **2010**, *132*, 2110.
- [122] H. Yu, K. Jo, K. L. Kounovsky, J. J. De Pablo, D. C. Schwartz, *J. Am. Chem. Soc.* **2009**, *131*, 5722.
- [123] S. Sengupta, D. Patra, I. Ortiz-Rivera, A. Agrawal, S. ShklyaeV, K. K. Dey, U. Córdova-Figueroa, T. E. Mallouk, A. Sen, *Nat. Chem.* **2014**, *6*, 415.
- [124] D. Pantarotto, W. R. Browne, B. L. Feringa, *Chem. Commun. (Camb)*. **2008**, 1533.
- [125] P. Schattling, B. Thingholm, B. Städler, *Chem. Mater.* **2015**, *27*, 7412.
- [126] L. K. E. A. Abdelmohsen, M. Nijemeisland, G. M. Pawar, G. J. A. Janssen, R. J. M. Nolte, J. C. M. Van Hest, D. A. Wilson, *ACS Nano* **2016**, *10*, 2652.
- [127] P. S. Schattling, M. A. Ramos-Docampo, V. Salgueiriño, B. Städler, *ACS Nano* **2017**, *11*, 3973.
- [128] K. K. Dey, X. Zhao, B. M. Tansi, W. J. Mendez-Ortiz, U. M. Cordova-Figueroa, R. Golestanian, A. Sen, W. J. Mandez-Ortiz, U. M. Cordova-Figueroa, R. Golestanian, A. Sen, *Nano Lett.* **2015**, *15*, 8311.
- [129] X. Ma, A. Jannasch, U. R. Albrecht, K. Hahn, A. Miguel-Lopez, E. Schaffer, S. Sanchez, *Nano Lett.* **2015**, *15*, 7043.

- [130] X. Ma, X. Wang, K. Hahn, S. Sánchez, *ACS Nano* **2016**, *10*, 3597.
- [131] X. Ma, A. C. Hortelao, A. Miguel-Lopez, S. Sanchez, *J. Am. Chem. Soc.* **2016**, *138*, 13782.
- [132] X. Chen, S. S. Mao, *Chem. Rev.* **2007**, *107*, 2891.
- [133] K. C. Popat, M. Eltgroth, T. J. LaTempa, C. A. Grimes, T. A. Desai, *Small* **2007**, *3*, 1878.
- [134] M. Safdar, J. Simmchen, J. Jänis, *Environ. Sci. Nano* **2017**, *4*, 1602.
- [135] Y. Hong, M. Diaz, U. M. Córdova-Fteueroa, A. Sen, *Adv. Funct. Mater.* **2010**, *20*, 1568.
- [136] S. Giudicatti, S. M. Marz, L. I. Soler, A. Madani, M. R. Jorgensen, S. Sanchez, O. G. Schmidt, *J. Mater. Chem. C* **2014**, *2*, 5892.
- [137] M. Enachi, M. Guix, V. Postolache, V. Ciobanu, V. M. Fomin, O. G. Schmidt, I. Tiginyanu, *Small* **2016**, *12*, 5497.
- [138] F. Mou, Y. Li, C. Chen, W. Li, Y. Yin, H. Ma, J. Guan, *Small* **2015**, *11*, 2564.
- [139] J. Palacci, S. Sacanna, S. Kim, G. Yi, D. J. Pine, P. M. Chaikin, *Phil. Trans. R. Soc.* **2014**, *372*, 20130372.
- [140] M. Murdoch, G. I. N. Waterhouse, M. A. Nadeem, J. B. Metson, M. A. Keane, R. F. Howe, J. Llorca, H. Idriss, *Nat. Chem.* **2011**, *3*, 489.
- [141] R. Dong, Q. Zhang, W. Gao, A. Pei, B. Ren, *ACS Nano* **2016**, *10*, 839.
- [142] B. Dai, J. Wang, Z. Xiong, X. Zhan, W. Dai, C.-C. Li, S.-P. Feng, J. Tang, *Nat. Nanotechnol.* **2016**, *11*, 1087.
- [143] D. P. Singh, U. Choudhury, P. Fischer, A. G. Mark, *Adv. Mater.* **2017**, *29*, 1701328.
- [144] S. Sundararajan, P. E. Lammert, A. W. Zudans, V. H. Crespi, A. Sen, *Nano Lett.* **2008**, *8*, 1271.
- [145] J. Burdick, R. Laocharoensuk, P. M. Wheat, J. D. Posner, J. Wang, *J. Am. Chem. Soc.* **2008**, *130*, 8164.

- [146] D. Kagan, R. Laocharoensuk, M. Zimmerman, C. Clawson, S. Balasubramanian, D. Kang, D. Bishop, S. Sattayasamitsathit, L. Zhang, J. Wang, *Small* **2010**, *6*, 2741.
- [147] S. Sundararajan, S. Sengupta, M. E. Ibele, A. Sen, *Small* **2010**, *6*, 1479.
- [148] L. Baraban, M. Tasinkevych, M. N. Popescu, S. Sanchez, S. Dietrich, O. G. Schmidt, *Soft Matter* **2012**, *8*, 48.
- [149] S. Sanchez, A. a. Solovev, S. M. Harazim, O. G. Schmidt, *J. Am. Chem. Soc.* **2011**, *133*, 701.
- [150] S. Sanchez, A. a. Solovev, S. Schulze, O. G. Schmidt, *Chem. Commun.* **2011**, *47*, 698.
- [151] S. Balasubramanian, D. Kagan, C. M. Jack Hu, S. Campuzano, M. J. Lobo-Castañon, N. Lim, D. Y. Kang, M. Zimmerman, L. F. Zhang, J. Wang, C. M. J. Hu, S. Campuzano, M. J. Lobo-Castanon, N. Lim, D. Y. Kang, M. Zimmerman, L. F. Zhang, J. Wang, *Angew. Chem. Int. Ed.* **2011**, *50*, 4161.
- [152] J. Orozco, S. Campuzano, D. Kagan, M. Zhou, W. Gao, J. Wang, *Anal. Chem.* **2011**, *83*, 7962.
- [153] S. Campuzano, J. Orozco, D. Kagan, M. Guix, W. Gao, S. Sattayasamitsathit, J. C. Claussen, A. Merkoçi, J. Wang, *Nano Lett.* **2012**, *12*, 396.
- [154] F. Kuralay, S. Sattayasamitsathit, W. Gao, A. Uygun, A. Katzenberg, *J. Am. Chem. Soc.* **2012**, *134*, 15217.
- [155] M. García, J. Orozco, M. Guix, W. Gao, S. Sattayasamitsathit, A. Escarpa, A. Merkoçi, J. Wang, *Nanoscale* **2013**, *5*, 1325.
- [156] J. Orozco, A. Cortés, G. Cheng, S. Sattayasamitsathit, W. Gao, X. Feng, Y. Shen, J. Wang, *J. Am. Chem. Soc.* **2013**, *135*, 5336.
- [157] G. Zhao, H. Wang, S. Sanchez, O. G. Schmidt, M. Pumera, *Chem. Commun.* **2013**, *49*, 5147.
- [158] M. Xuan, J. Shao, X. Lin, L. Dai, Q. He, *ChemPhysChem* **2014**, *15*, 2255.
- [159] F. Peng, Y. Tu, J. C. M. Van Hest, D. A. Wilson, *Angew. Chem. Int. Ed.* **2015**, *54*,


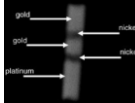

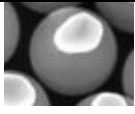
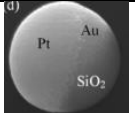
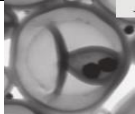


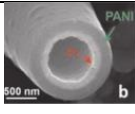
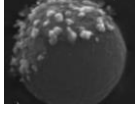

- 11662.
- [160] Y. Tu, F. Peng, A. A. M. André, Y. Men, M. Srinivas, D. A. Wilson, *ACS Nano* **2017**, *11*, 1957.
- [161] F. Z. Mou, C. R. Chen, Q. Zhong, Y. X. Yin, H. R. Ma, J. G. Guan, *ACS Appl. Mater. Interfaces* **2014**, *6*, 9897.
- [162] J. Li, P. Angsantikul, W. Liu, B. Esteban-Fernandez de Avila, S. Thamphiwatana, M. Xu, E. Sandraz, X. Wang, J. Delezuk, W. Gao, L. Zhang, J. Wang, *Angew. Chem. Int. Ed.* **2017**, *56*, 2156.
- [163] J. Li, S. Thamphiwatana, W. Liu, B. Esteban-Fernandez De Avila, P. Angsantikul, E. Sandraz, J. Wang, T. Xu, F. Soto, V. Ramez, X. Wang, W. Gao, L. Zhang, J. Wang, *ACS Nano* **2016**, *10*, 9536.
- [164] C. Chen, E. Karshalev, J. Li, F. Soto, R. Castillo, I. Campos, F. Mou, J. Guan, J. Wang, *ACS Nano* **2016**, *10*, 10389.
- [165] J. R. Baylis, J. H. Yeon, M. H. Thomson, A. Kazerooni, X. Wang, A. E. St. John, E. B. Lim, D. Chien, A. Lee, J. Q. Zhang, J. M. Piret, L. S. Machan, T. F. Burke, N. J. White, C. J. Kastrup, *Sci. Adv.* **2015**, *1*, e1500379.
- [166] Z. Wu, X. Lin, X. Zou, J. Sun, Q. He, *ACS Appl. Mater. Interfaces* **2015**, *7*, 250.
- [167] Y. Wu, X. Lin, Z. Wu, H. Möhwald, Q. He, *ACS Appl. Mater. Interfaces* **2014**, *6*, 10476.
- [168] J. P. Celli, B. S. Turner, N. H. Afdhal, R. H. Ewoldt, G. H. McKinley, R. Bansil, S. Erramilli, S. Erramilli, *Biomacromolecules* **2007**, *8*, 1580.
- [169] D. Walker, B. T. Kasdorf, H.-H. Jeong, O. Lieleg, P. Fischer, *Sci. Adv.* **2015**, *1*, e1500501.
- [170] E. Morales-Narváez, M. Guix, M. Medina-Sánchez, C. C. Mayorga-Martinez, A. Merkoçi, *Small* **2014**, *10*, 2542.
- [171] D. Vilela, J. Orozco, G. Cheng, S. Sattayasamitsathit, M. Galarnyk, C. Kan, J. Wang,

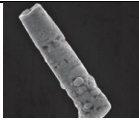
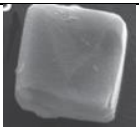

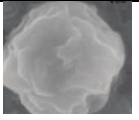

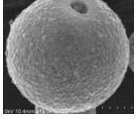


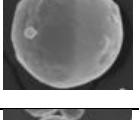
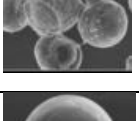


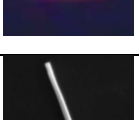
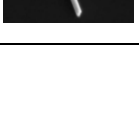
- A. Escarpa, *Lab Chip* **2014**, *14*, 3505.
- [172] X. Yu, Y. Li, J. Wu, H. Ju, *Anal. Chem.* **2014**, *86*, 4501.
- [173] B. E. F. de Ávila, M. Zhao, S. Campuzano, F. Ricci, J. M. Pingarrón, M. Mascini, J. Wang, *Talanta* **2017**, *167*, 651.
- [174] M. M. Khin, A. S. Nair, V. J. Babu, R. Murugan, S. Ramakrishna, *Energy Environ. Sci.* **2012**, *5*, 8075.
- [175] J. G. S. Moo, H. Wang, G. Zhao, M. Pumera, *Chem. Eur. J.* **2014**, *20*, 4292.
- [176] J. Orozco, V. Garcia-Gradilla, M. D'Agostino, W. Gao, A. Cortes, J. Wang, *ACS Nano* **2013**, *7*, 818.
- [177] V. V. Singh, K. Kaufmann, B. Esteban-Fernandez de Avila, M. Uygun, J. Wang, B. Esteban-Fernández de Ávila, M. Uygun, J. Wang, *Chem. Commun.* **2016**, *52*, 3360.
- [178] B. Jurado-Sánchez, A. Escarpa, J. Wang, *Chem. Commun.* **2015**, *51*, 14088.
- [179] V. V. Singh, K. Kaufmann, J. Orozco, J. Li, M. Galarnyk, G. Arya, J. Wang, *Chem. Commun.* **2015**, *51*, 11190.
- [180] S. Cinti, G. Valdés-Ramírez, W. Gao, J. Li, G. Palleschi, J. Wang, *Chem. Commun.* **2015**, *51*, 8668.
- [181] M. Guix, J. Orozco, M. Garcia, W. Gao, S. Sattayasamitsathit, A. Merkoçi, A. Escarpa, J. Wang, *ACS Nano* **2012**, *6*, 4445.
- [182] T. Do Minh, M. Safdar, J. Janis, *Chem. Eur. J.* **2017**, *23*, 8134.
- [183] L. Soler, V. Magdanz, V. M. Fomin, S. Sanchez, O. G. Schmidt, *ACS Nano* **2013**, *7*, 9611.
- [184] J. Parmar, D. Vilela, E. Pellicer, D. Esque-de los Ojos, J. Sort, S. Sanchez, *Adv. Funct. Mater.* **2016**, *26*, 4152.
- [185] O. M. Wani, M. Safdar, N. Kinnunen, J. Jänis, *Chem. Eur. J.* **2016**, *22*, 1244.
- [186] F. Perreault, A. Fonseca de Faria, M. Elimelech, *Chem. Soc. Rev.* **2015**, *44*, 5861.
- [187] J. Orozco, L. A. Mercante, R. Pol, A. Merkoçi, *J. Mater. Chem. A* **2016**, *4*, 3371.

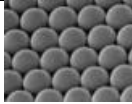
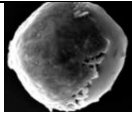
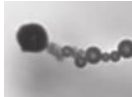



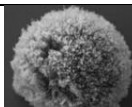

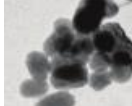
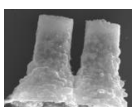

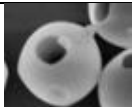

- [188] D. Vilela, J. Parmar, Y. Zeng, Y. Zhao, S. Sanchez, *Nano Lett.* **2016**, *16*, 2860.
- [189] D. A. Uygun, B. Jurado-Sánchez, M. Uygun, J. Wang, *Environ. Sci. Nano* **2016**, *3*, 559.
- [190] J. Li, V. V Singh, S. Sattayasamitsathit, J. Orozco, K. Kaufmann, R. Dong, W. Gao, B. Jurado-sanchez, Y. Fedorak, J. Wang, *ACS Nano* **2014**, *8*, 11118.
- [191] J. A. M. Delezuk, D. E. Ramírez-Herrera, B. Esteban-Fernández de Ávila, J. Wang, *Nanoscale* **2017**, *9*, 2195.
- [192] T. Li, L. Li, W. Song, L. Wang, G. Shao, G. Zhang, *ECS J. Solid State Sci. Technol.* **2015**, *4*, S3016.
- [193] V. V. Singh, A. Martin, K. Kaufmann, S. D. S. De Oliveira, J. Wang, *Chem. Mater.* **2015**, *27*, 8162.
- [194] B. Jurado-Sánchez, S. Sattayasamitsathit, W. Gao, L. Santos, Y. Fedorak, V. V. Singh, J. Orozco, M. Galarnyk, J. Wang, *Small* **2015**, *11*, 499.
- [195] M. M. Abu-Khader, *Energy Sources Part A-Recovery Util. Environ. Eff.* **2006**, *28*, 1261.
- [196] M. Uygun, V. V. Singh, K. Kaufmann, D. A. Uygun, S. D. S. De Oliveira, J. Wang, *Angew. Chem. Int. Ed.* **2015**, *54*, 12900.
- [197] V. V. Singh, F. Soto, K. Kaufmann, J. Wang, *Angew. Chem. Int. Ed.* **2015**, *54*, 6896.
- [198] J. Li, O. E. Shklyae, T. Li, W. Liu, H. Shum, I. Rozen, A. C. Balazs, J. Wang, *Nano Lett.* **2015**, *15*, 7077.
- [199] C. C. Mayorga-Martinez, J. G. S. Moo, B. Khezri, P. Song, A. C. Fisher, Z. Sofer, M. Pumera, *Adv. Funct. Mater.* **2016**, *26*, 6662.
- [200] X. Zhang, Z. Liu, *Nat. Mater.* **2008**, *7*, 435.
- [201] W. Adams, M. Sadatgol, D. Guney, *AIP Adv.* **2016**, *6*, 100701.
- [202] J. Li, W. Liu, T. Li, I. Rozen, J. Zhao, B. Bahari, B. Kante, J. Wang, *Nano Lett.* **2016**, *16*, 6604.

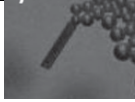
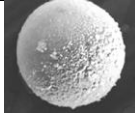
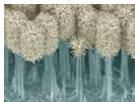
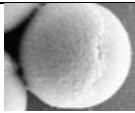
[203] J. Li, W. Gao, R. Dong, A. Pei, S. Sattayasamitsathit, J. Wang, *Nat. Commun.* **2014**, *5*, 5026.

Table 1. A summary of catalytic materials explored for MNMs preparation.

Catalyst Materials	Composition	Geometry	Propulsion Mechanisms	Fuel (%)	Speed (bdl s ⁻¹)	Appearance of MNMs	Selected References
Pt	Pt/Au	Nanorods	Self-electrophoresis	H ₂ O ₂	2-10		[21]
	Pt/Ni/Au/Ni/Au	Nanorods	Self-electrophoresis	H ₂ O ₂	3		[28]
	CNT-Pt/Au	Nanorods	Self-electrophoresis	H ₂ O ₂	100	-	[29]
	Pt/PS	Janus particles	Self-diffusiophoresis	H ₂ O ₂	2	-	[16]
	Pt/SiO ₂	Janus particles	Self-diffusiophoresis	H ₂ O ₂	7		[37]
	Pt NP/SiO ₂	Janus particles	Self-diffusiophoresis	H ₂ O ₂	6		[38]
	Pt/Au/SiO ₂	Janus Particles	Self-electrophoresis	H ₂ O ₂	1.5		[39]
	Pt NPs@PS- <i>b</i> -PEG	NP loaded stomatocyte	Bubble thrust, Self-diffusiophoresis	H ₂ O ₂	115		[51]
	Pt/Au/Fe/Ti	Tubular	Bubble propulsion	H ₂ O ₂	1		[56]
	Pt/Cr/Ti	Tubular	Bubble propulsion	H ₂ O ₂	200		[68]
	Pt/PEDOT	Tubular	Bubble-induced propulsion	H ₂ O ₂	350		[61]
Ag	Ag NPs /Polymer bead	Janus particles	Self-diffusiophoresis	H ₂ O ₂	1.5		[77]
	Ag NPs/PCL	Sheet-like	Bubble propulsion	H ₂ O ₂	5		[78]

	Ag/Cu	Tubular	Bubble propulsion	H ₂ O ₂	20		[79]
	Ag/Zeolite	Janus particles	Bubble propulsion	H ₂ O ₂	30		[80]
MnOx	MnO ₂ NPs /paper	Tubular	Bubble propulsion	H ₂ O ₂	5.5		[86]
	MnOx-GOx	Crumples	Bubble propulsion	H ₂ O ₂	-		[84]
	MnO ₂ -GOx	Sheet-like	Bubble propulsion	H ₂ O ₂	27		[85]
	ε-MnO ₂	Hollow Spherical particles	Bubble propulsion	H ₂ O ₂	200		[89]
Zn	Zn/PANI	Tubular	Bubble propulsion	Acids	100		[92]
	Zn/PEDOT	Tubular	Bubble propulsion	Acids	5		[94]
	Zn/Fe	Particles	Bubble propulsion	Acids	1.5		[164]
Mg	Mg/Pt	Particles	Bubble propulsion	H ₂ O	4		[95]
	Mg/Ti/Au	Particles	Bubble propulsion	H ₂ O	3		[190]
	Mg@Au/PEDO T	Particles loaded in tubes	Bubble propulsion	H ₂ O	5		[163]
Ni	Ni/Au	Nanorods	Self-electrophoresis	H ₂ O ₂	-		[97]
	Ni-Fe/Au	Nanowires	Bubble propulsion	H ₂ O ₂ , hydrazine	157		[98]

Ir	Ir/SiO ₂	Janus particles	Self-diffusiophoresis	Hydrazine	20		[99]
Al, Pd	Al-Ga/Ti	Janus particles	Bubble propulsion	H ₂ O	150		[100]
	Al-Pd	Janus particles	Bubble propulsion	Acid, base, H ₂ O ₂	10		[101]
Ru	Ru/Au	Nanorods	Self-electrophoresis	H ₂ O ₂	11	-	[102]
	Au-Ru-Au	Nanorods	Self-electrophoresis	H ₂ O ₂	2		[104]
Fe	Fe ⁰	NP aggregates	Bubble propulsion	Citric acid	-		[109]
	Fe/Au/PEDOT	Tubular	Bubble propulsion	Acid	4.4		[110]
Ca	CaC ₂	Particles	Bubble propulsion	Water	8	-	[111]
	CaCO ₃ /Co	Particles	Particle dissolution	Mild Acid	0.5		[112]
Enzymes	Catalase/Au/Ti	Tubular	Bubble propulsion	H ₂ O ₂	10		[114]
	Catalase/SiO ₂ -Ni	Cluster	Bubble propulsion	H ₂ O ₂	-		[116]
	Catalase/AuNPs/albumin/poly-L-lysine	Tubular	Bubble propulsion	H ₂ O ₂	6		[166]
	Glucose oxidase/SiO ₂	Hollow particles	Chemo-phoresis	Glucose	-		[129]
	Urease/SiO ₂	Hollow particles	Chemo-phoresis	Urea	5		[130]
	Urease/SiO ₂	Tubular	Flow of the reaction products	Urea	2.8		[131]

TiO ₂	Anatase-TiO ₂	Tubular	Bubble propulsion	H ₂ O ₂ , UV light	2.5		[138]
	TiO ₂ /Au	Janus particles	Self-electrophoresis	Water, H ₂ O ₂ , UV light	25		[141]
	TiO ₂ /Si@Pt NPs	Nanotree	Self-electrophoresis	H ₂ O ₂ , Benzoquinone /hydroquinone	-		[142]
	TiO ₂ /SiO ₂	Janus particles	Self-diffusiophoresis	H ₂ O ₂	3-5		[143]

Catalytic micro- and nanomotors are tiny devices that can autonomously propel in the presence of a chemical fuel. This progress report presents an overview of the achievements towards the discovery of new materials and approaches to achieve efficient motion in different chemical fuels. The motion can be utilized to perform various tasks for biomedical and environmental applications.

